



HAL
open science

Spin state and deep interior structure of Mars from InSight radio tracking

Sébastien Le Maistre, Attilio Rivoldini, Alfonso Caldiero, Marie Yseboodt, Rose-Marie Baland, Mikael Beuthe, Tim van Hoolst, Véronique Dehant, William M. Folkner, Dustin Buccino, et al.

► **To cite this version:**

Sébastien Le Maistre, Attilio Rivoldini, Alfonso Caldiero, Marie Yseboodt, Rose-Marie Baland, et al.. Spin state and deep interior structure of Mars from InSight radio tracking. *Nature*, 2023, 619, pp.733-737. <10.1038/s41586-023-06150-0>. <insu-04187889>

HAL Id: insu-04187889

<https://insu.hal.science/insu-04187889v1>

Submitted on 16 Nov 2023

HAL is a multi-disciplinary open access archive for the deposit and dissemination of scientific research documents, whether they are published or not. The documents may come from teaching and research institutions in France or abroad, or from public or private research centers.

L'archive ouverte pluridisciplinaire **HAL**, est destinée au dépôt et à la diffusion de documents scientifiques de niveau recherche, publiés ou non, émanant des établissements d'enseignement et de recherche français ou étrangers, des laboratoires publics ou privés.



HAL Authorization

Spin state and deep interior structure of Mars from InSight radio tracking

Authors: Sébastien Le Maistre^{1,2*}, Attilio Rivoldini¹, Alfonso Caldiero^{1,2}, Marie Yseboodt¹, Rose-Marie Baland¹, Mikael Beuthe¹, Tim Van Hoolst^{1,3}, Véronique Dehant^{1,2}, William M. Folkner⁴, Dustin Buccino⁴, Daniel Kahan⁴, Jean-Charles Marty⁵, Daniele Antonangeli⁶, James Badro⁷, Mélanie Drilleau⁸, Alex Konopliv⁴, Marie-Julie Péters¹, Ana-Catalina Plesa⁹, Henri Samuel⁷, Nicola Tosi⁹, Mark Wieczorek¹⁰, Philippe Lognonné⁷, Mark Panning⁴, Suzanne Smrekar⁴, W. Bruce Banerdt⁴.

Affiliations:

¹ Royal Observatory of Belgium, Brussels, Belgium.

² UCLouvain, Louvain-la-Neuve, Belgium.

³ Institute of Astronomy, KU Leuven, Leuven, Belgium.

⁴ Jet Propulsion Laboratory, California Institute of Technology, Pasadena, USA.

⁵ Centre national d'Études Spatiales, Toulouse, France.

⁶ IMPMC, Sorbonne Université, MNHN, CNRS, Paris, France.

⁷ Université de Paris, Institut de Physique du Globe de Paris, CNRS, Paris, France.

⁸ Institut Supérieur de l'Aéronautique et de l'Espace SUPAERO, Toulouse, France.

⁹ DLR Institute of Planetary Research, Berlin, Germany.

¹⁰ Université Côte d'Azur, Observatoire de la Côte d'Azur, CNRS, Laboratoire Lagrange, Nice, France.

* sebastien.lemaistre@oma.be, Royal Observatory of Belgium, 3 avenue Circulaire, B1180 Brussels, Belgium.

Abstract

Knowledge of the interior structure and atmosphere of Mars is essential to understand how the planet formed and evolved. A major obstacle to probe planetary interiors is that they are not directly accessible and that most geophysical data provide global information that cannot be uniquely related to the core, mantle, or crust separately. The NASA InSight mission changed this situation by providing for the first time high quality seismic and lander radio science data^{1,2}. Here we determine fundamental properties of the core, mantle, and atmosphere of Mars by precisely measuring the planet's rotation. We detect a resonance with a rotational normal mode in InSight's radio science data that allows us to characterize the core and mantle separately. For an entirely solid mantle, we found that the liquid core has a radius of 1835 ± 55 km and a mean density of $5955\text{-}6290$ kg/m³, and that the density jump at

the core-mantle boundary is 1690-2110 kg/m³. Our analysis of InSight's radio tracking data argues against the existence of a solid inner core and reveals the shape of the core, which indicates that internal mass anomalies exist deep within the mantle. We also find evidence of a secular acceleration in the Martian rotation rate, which could be the expression of a long-term trend in the internal dynamics of Mars or in its atmosphere and ice caps.

The RISE Experiment

In order to probe the planet's deep interior and atmosphere dynamics, the radio-science experiment RISE (Rotation and Interior Structure Experiment) of the NASA's InSight mission (Interior exploration using Seismic Investigations, Geodesy, and Heat Transport) measures the Doppler shift (or range rate) induced by tiny variations in the rotation and orientation of Mars^{1,2} on the two-way radio links, enabled by RISE's X-band coherent transponder, between its two medium-gain antennas and the NASA Deep Space Network.

The RISE experiment accurately characterizes the rotation and orientation parameters of Mars and was specifically designed to measure the Martian nutations, periodic motions of the spin axis in space³, in order to study the core. For each forcing frequency ω ($\omega > 0$) expressed in the inertial frame, the nutation can be decomposed into prograde (P') and retrograde (R') circular motions. Their amplitudes are expressed as^{3,4,5}

$$P'(\omega) = T_F(\omega) P(\omega) \text{ and } R'(\omega) = T_F(-\omega) R(\omega), \quad (1)$$

where P and R are the prograde and retrograde nutation amplitudes of a rigid Mars model, while the transfer function T_F describes the dependence on the interior structure. For an entirely fluid core (Supplementary Section 3), the nutation amplitudes are resonantly amplified by the Free Core Nutation (FCN), a normal mode related to the misalignment between the core and mantle rotation axes, according to^{3,6}

$$T_F(\omega) = 1 + F \frac{\omega}{\omega - \omega_{FCN}}, \quad (2)$$

where F is the core amplification factor and ω_{FCN} is the FCN frequency. These transfer function parameters are related to the interior structure of the planet by

$$F = \frac{A_f}{A - A_f} \left(1 - \frac{\gamma}{e}\right) \text{ and } \omega_{FCN} = -\Omega \frac{A}{A - A_f} (e_f - \beta). \quad (3)$$

Nutation amplitudes thus depend on the mean equatorial moments of inertia of the fluid core (A_f) and mantle ($A - A_f$), the dynamical polar flattenings of the whole planet ($e = (C - A)/A$ with A and C the mean equatorial and polar moments of inertia of Mars) and of the core ($e_f = (C_f - A_f)/A_f$ with C_f the polar moment of inertia of the core), the deformation of the core induced by the tidal forcing (γ), and the deformation of the core due to its differential rotation with respect to the mantle (β). Nutation analysis based on radiometric measurements is the only technique that can provide direct estimates of these properties of the Martian core. Nutations can also be affected by triaxiality, core-mantle boundary coupling, and other rotation normal modes³. However, all those effects are small for Mars and are therefore neglected here (Supplementary Section 9).

The Doppler measurements are analyzed with two different orbitography software, MONTE⁷ and GINS^{8,9} (Supplementary Section 1), using *a priori* values for the rotation and polar motion parameters from Konopliv *et al.* (2020)¹⁰ and for the rigid nutation parameters from Baland *et al.* (2020)¹¹ (Methods). Prior transfer function parameters are taken within a large range of values (Supplementary Section 2). To be able to decorrelate the precession rate and the orientation of the spin axis at epoch, we also consider Viking data in addition to 30 months of more accurate RISE tracking data (Methods).

Mars rotation and orientation estimates

The estimated rotation/orientation parameters converge after 600 days of operations (see Fig. 1) and even sooner for the precession rate, thanks to the combination of Viking and RISE data (Supplementary Section 4).

Separate analyses of Viking and RISE data lead to incompatible estimates of the rotation parameters. We therefore estimate separate sets of seasonal spin series for each mission, along with a quadratic term ($\ddot{\phi}$) modeling a spin acceleration. Our estimate of $\ddot{\phi} = 4.11 \cdot 10^{-12} \pm 9.1 \cdot 10^{-13} \text{deg/day}^2$ (Fig. 1a), the first secular trend detected in the Martian rotation rate, translates into a decrease of length of day of Mars of $7.6 \cdot 10^{-4} \text{ms/year}$, which corresponds to a rotational acceleration of $4.0 \pm 0.9 \text{mas/year}^2$, three orders of magnitude larger than that due to Phobos tides and than the expected deceleration by the Sun. This rotational acceleration could be the expression of a long term trend in the internal dynamics of Mars or in its atmosphere and ice caps. A secular variation of the degree-2 gravity zonal coefficient $\dot{J}_2 = -4.4 \cdot 10^{-12}$ over one Martian year (an order of magnitude smaller than for the Earth) would be consistent with the observed acceleration and could be related to postglacial rebound. It could also result from a secular accumulation of ice at the polar caps (<4cm per Earth year above the 80°N latitude of the permanent cap) leading to a decrease of the atmospheric pressure of less than 0.1 Pa per Martian year, which is below the 1.5 Pa absolute error of the InSight APSS pressure sensor¹².

We detect for the first time the small motions ($\leq 40 \text{cm}$) of a lander in inertial space due to the effect on nutations of the Martian liquid core and obtain estimates for the nutation parameters $F = 0.0615 \pm 0.007$ and $\tau_{FCN} = 2\pi/\omega_{FCN} = -243 \pm 3.3 \text{days}$ (Fig. 1cd). Our estimated precession rate, $\dot{\psi} = -7598.1 \pm 2.2 \text{mas/year}$ (Fig. 1b), corresponds to a normalized polar moment of inertia of 0.36419 ± 0.00011 (Supplementary Section 5). New constraints on the core of Mars can be derived from these values by using a set of interior structure models.

Constraints on Mars interior structure

We consider two temperature profiles (hot and cold), which are representative end-members of a set of profiles inferred from InSight seismic data (Methods). For the mantle composition, we use the EH45 model of Sanloup *et al.* (1999)¹³ and the model of Yoshizaki and McDonough (2020)¹⁴ (denoted by YMD), which are based on analyses of Martian meteorites and are representative of upper and lower limits in the FeO content of published mantle compositions^{e.g.15}, which directly relates to mantle's density. Our structure models agree with the crustal structure inferred from seismic data (Supplementary Section 8). Mantle

anelasticity, which affects the complex compliances β and γ , is parameterized with a frequency dependent model for shear dissipation (Supplementary Section 9). Given that τ_{FCN} and F have a relatively small dependence on the composition and thermal state of the liquid core, they are computed under the assumption that the core is a convecting liquid iron-sulfur alloy (Supplementary Section 12).

Since the estimated core factor F differs from zero at more than 8σ , the core beneath the solid mantle must be liquid. This independently confirms previous inferences from tidal measurements¹⁶ and seismic observations¹⁷. From F we determine $A_f = (0.0286 \pm 0.0033) m_a r_a^2$ (Supplementary Section 13). F (Fig. 2b) is nearly independent of the flattening, mantle temperature, and composition of the core, and is therefore well suited to determine the radius R_c of the fluid core. We find that $R_c = 1835 \pm 55$ km, in good agreement with previous results based on geodesy data^{e.g.18,19} and reflected seismic waves from the core-mantle boundary¹⁷. The radius of the fluid metallic core, however, could possibly be more than 200 km smaller if the lowest part of the mantle is molten and rotates independently from the solid mantle above (Supplementary Section 11).

Interpreting the FCN period in terms of interior structure requires identifying plausible processes that can explain the flattening of the core (Eq.3). The simplest model matching the surface flattening consists in assuming two mass-sheet anomalies, one associated with the surface topography and another emplaced deeper in the lithosphere²⁰. The latter could result from relief along the crust-mantle interface (Moho) and from horizontal density variations due to temperature variations. Additional effects on the core flattening can be due to density anomalies in the convecting mantle^{21,22} and stable boundary layers, thermal or chemical, at the bottom of the mantle²³. We construct models with two or three mass anomalies acting as static loads: at the surface, at the Moho or at the bottom of the lithosphere, and possibly at the bottom of the mantle. The depth of the second load significantly affects the shape of the core (Supplementary Section 10).

Models that only consider a second load placed at the Moho require a core radius smaller than about 1760 km, outside the range inferred from F at 1σ (Fig.2a,c). Models with a load placed at the bottom of the lithosphere require a relatively thick lithosphere (600 km) to agree with both τ_{FCN} and F , and therefore a crust highly enriched in heat producing elements compared to the mantle (Supplementary Section 7). Temperature profiles directly inferred from seismic data¹⁷ show that the lithosphere can be up to 200 km thinner (Supplementary Section 7) and many models based on these profiles are not compatible with RISE data unless a third load is emplaced at the bottom of the mantle (analogous to the Large Low Shear Velocity Provinces on Earth^{e.g.24}) (Fig. 2 a,c). Models with a thinner lithosphere can also be reconciled with τ_{FCN} if a fluid dense basal layer is present at the bottom of the mantle (Supplementary Section 11).

The FCN period indicates a density jump of 1690-2110 kg/m³ at the core-mantle boundary (Fig. 3), and the size of the core radius implies a mean density of 5955-6290 kg/m³ (Fig. S8), in the upper range of values proposed in Stähler *et al.* (2021)¹⁷, requiring a significant amount of light elements alloyed with iron (Fig. 4). The most prominent candidate for a light element is sulfur (S), an abundant and highly siderophile element at core forming conditions, with a

concentration likely below ~20wt% according to cosmochemistry^{e.g.14,25}. S alloying to Fe during core differentiation comes with a few wt% of oxygen (O)²⁶ making liquid Fe-O-S the chemically simplest plausible composition. However, if the S concentration in the core lies within the range predicted by cosmochemistry, a Fe-O-S core is possible only if its radius is at the lower end of our estimate and its temperature is high (Fig. 4). Larger core radii require the presence of additional light elements, such as hydrogen (H) and carbon (C)^{e.g.14,25,27,28}, or an S content equivalent to EH chondrites. Given the limited solubility of carbon in liquid Fe-S^{e.g.29}, the composition of the core favored by RISE consists of 2.5±0.5 wt%O, 15±2 wt%S, 1.5±0.5 wt%C, if 1wt% of H is assumed (Fig. 4). A lower amount of light elements is possible if Mars has a fully molten lower mantle layer²³.

The large amount of light elements, with an S fraction close to the Fe-S eutectic, results in a liquidus significantly below the expected core temperature (Supplementary Section 12). An inner core is therefore highly unlikely. If an inner core were nevertheless to exist, another rotational mode named the Free Inner Core Nutation could affect the ½-annual or ⅓ annual prograde nutation³⁰. No such signature has been detected in the RISE data (Supplementary Section 3). The absence of an inner core is also in agreement with the early cessation of an internally generated magnetic field^{e.g.31}.

References from main text

1. Banerdt, W. B. *et al.*, Initial results from the InSight mission on Mars, *Nat. Geosci.* **13**, 183–189 (2020).
2. Folkner, W. M. *et al.*, The rotation and interior structure experiment on the InSight mission to Mars, *Space Sci. Rev.* **214** (5), 100 (2018).
3. Dehant, V., Mathews, P.M., Ed., Precession, Nutation and Wobble of the Earth, *Cambridge University Press*, Cambridge (2015).
4. Sasao, T. *et al.*, A simple theory on dynamical effects of stratified fluid core upon nutational motion of the Earth, *Proc. IAU Symposium* **78**, 165–183 (1980).
5. Folkner, W. M. *et al.*, Interior structure and seasonal mass redistribution of Mars from radio tracking of Mars pathfinder, *Science* **278** (5344), 1749–1752 (1997).
6. Yoder, C.F., Standish, E.M., Martian precession and rotation from Viking lander range data, *J. Geophys. Res.* **102**(E2), 4065–4080 (1997).
7. Evans, S. *et al.*, MONTE: The next generation of mission design and navigation software, *CEAS Space J.* **10**, 79–86 (2018).
8. Marty, J.-C. *et al.*, GINS: The CNES/GRGS GNSS scientific software, *3rd Int. Coll. Sci. Fundam. Asp. Galileo Program. ESA proceedings WPP326* **31**, 8-10 (2011).
9. Le Maistre, S. *et al.*, Lander radio science experiment with a direct link between Mars and the Earth, *Planet. Space Sci.* **68**, 105–122 (2012).
10. Konopliv, A. S. *et al.*, Detection of the Chandler Wobble of Mars From Orbiting Spacecraft, *Geophys. Res. Lett.* **47**, e2020GL090568 (2020).
11. Baland, R.-M. *et al.*, The precession and nutations of a rigid Mars, *Celest Mech Dyn Astr* **132**, 47 (2020).

12. Banfield, D. et al., InSight Auxiliary Payload Sensor Suite (APSS), *Space Sci. Rev.* **215**(1), 1-33 (2019).
13. Sanloup, C. et al., Density measurements of liquid Fe-S alloys at high pressure, *Geophys. Res. Lett.* **27**, 811 (1999).
14. Yoshizaki, T., McDonough, W. F., The composition of Mars *Geochim. Cosmochim. Acta* **273**, 137–162 (2020).
15. Smrekar, S.E. et al., Pre-mission InSights on the Interior of Mars, *Space Sci Rev.* **215**, 3 (2019).
16. Yoder, C. F. et al., Fluid core size of Mars from detection of the solar tide, *Science* **300**, 299–303 (2003).
17. Stähler, S. C. et al., Seismic detection of the martian core, *Science* **373**, 443–448 (2021).
18. Rivoldini, A. et al., Geodesy constraints on the interior structure and composition of Mars, *Icarus* **213**, 451–472 (2011).
19. Khan, A. et al., A geophysical perspective on the bulk composition of Mars, *J. Geophys. Res.* **123**, 575–611 (2018).
20. Wiczorek, M. A., Beuthe, M., Rivoldini, A., Van Hoolst, T., Hydrostatic interfaces in bodies with nonhydrostatic lithospheres, *J. Geophys. Res. Planets* **124**, 1410–1432 (2019).
21. Kiefer, W.S., Bills, B.G., Nerem, R.S., An inversion of gravity and topography for mantle and crustal structure on Mars, *J. Geophys. Res. Planets* **101**, 9239 (1996).
22. Defraigne, P., Dehant, V., Van Hoolst, T., Steady-state convection in Mars' mantle, *Planet. Space Sci.*, **49**, 501–509 (2001).
23. Samuel, H. et al., The Thermo-Chemical Evolution of Mars With a Strongly Stratified Mantle, *J. Geophys. Res. Planets* **126**, e2020JE006613 (2021).
24. McNamara, A. K., A review of large low shear velocity provinces and ultra low velocity zones, *Tectonophysics* **760**, 199–220 (2019).
25. Steenstra, E. S., van Westrenen, W., A synthesis of geochemical constraints on the inventory of light elements in the core of Mars, *Icarus* **315**, 69–78 (2018).
26. Gendre, H. et al., Martian core composition from experimental high-pressure metal-silicate phase equilibria, *Geochemical Perspectives Letters*, **21** (2022).
27. Shibasaki, Y. et al., Hydrogen partitioning between iron and ringwoodite: Implications for water transport into the Martian core, *Earth Planet. Sci. Lett.* **287**, 463–470 (2009).
28. Zharkov, V.N., The Internal Structure of Mars: A Key to Understanding the Origin of Terrestrial Planets, *Sol. Syst. Res.* **30**, 456-46 (1996).
29. Tsuno, T., Frost, D.J., Rubie, D.C., The effects of nickel and sulphur on the core-mantle partitioning of oxygen in Earth and Mars, *Phys. Earth Planet. Inter.* **185**, 1–12 (2011).
30. Defraigne, P., Rivoldini, A., Van Hoolst, T., Dehant, V., Mars nutation resonance due to free inner core nutation, *J. Geophys. Res. Planets* **108**(E12), 5128 (2003).
31. Mittelholz, A. et al., Timing of the martian dynamo: New constraints for a core field 4.5 and 3.7 Ga ago, *Sci. Adv.* **6**, 18 (2020).
32. Lodders, K., Relative atomic solar system abundances, mass fractions, and atomic masses of the elements and their isotopes, composition of the solar photosphere, and compositions of the major chondritic meteorite groups, *Space Sci Rev.* **217**(3), 44 (2021).

Main figures legends

Figure 1: Main rotation parameters estimates. Converging solutions of the quadratic rotation coefficient (a), precession rate (b), core amplification factor (c), and FCN period (d) as a function of time after InSight landing. Horizontal lines are the preferred solutions of this paper (Extended Data Table 2). Shaded regions are formal uncertainties (1σ).

Figure 2: Interpretation of nutation parameters in terms of interior structure. (a) Core radius versus τ_{FCN} , (b) core radius versus F , and (c) correlation between τ_{FCN} and F , for models based on YMD¹⁴ mantle composition (colored areas), and models with a stable magma layer at the bottom of the mantle (circles). Colors differentiate models with one internal load at the Moho (green) or at the bottom of the lithosphere (blue), or with two internal loads located at the Moho and at the bottom of the mantle (orange). Blue and green lines are hidden behind orange lines in (b). All models include a surface load associated with the shape of Mars. Solid (dashed) lines represent the hot (cold) end-member mantle temperature model. Gray shaded areas represent 1σ , 2σ , and 3σ uncertainties.

Figure 3: Density jump at the core-mantle boundary as function of FCN period for the YMD mantle composition¹⁴. Models that agree with F (1σ) are represented by thick lines. Colors and dashing as in Fig. 2.

Figure 4: Fraction of light elements in the core of Mars. Sulfur concentration in the core as a function of core radius for the YMD mantle model (thick lines) and EH45 (thin line, only Fe-O-S with T_{hot}) mantle models, and for different core compositions. Dotted (full) curves show models based on cold (hot) mantle temperature. The gray area represents the core radius inferred from this study (1σ). The darker purple area is the S content (core mass fraction dependent) predicted from cosmochemical considerations²⁴ and the lighter purple area assumes that the S content of Mars is equivalent to chondrites (1.6-5.6 wt%)³². The inset shows the wt% of O associated with each model. YMD models based on T_{cold} only match the MOI if the core radius is smaller than 1865 km and EH45 models based on T_{hot} models match the MOI if the core is smaller than 1840 km (Supplementary Section 8).

Methods

Radio-tracking data

The RISE data used cover the period from Nov 27, 2018 to May 31, 2021, corresponding to 915 Earth days (890 Sols). Viking lander 1 data are also used, mostly to decorrelate the rates and angles at J2000 epoch, while Mars Pathfinder and Mars Exploration Rovers data are not used because they are scattered and few in number compared to RISE data (see Extended Data Table 1).

544 tracking passes of RISE are analyzed, corresponding to ~25000 Doppler observable data points averaged over 60 seconds: with ~16150 data points for the East antenna and ~8900 data points for the West antenna. The nominal pass length of 60 minutes was reduced to 30 minutes after 600 days of mission because of the decrease in the energy available on the InSight lander. The number of passes each week has also decreased from 5-7 to 1-3 for the same reason. The antennas are mounted on top of the main deck with fixed East/West pointing directions. The Earth azimuthal range covered is 77°-130° for the East and 246°-299° for the West antenna. The Earth's elevation at the lander is between 10° and 49°.

Besides the instrumental noise of the RISE instrumentation and the DSN station, the quality of RISE data also depends on the Sun-Earth-Probe (SEP) angle, the line-of-sight (LOS) geometry (especially the LOS elevation above the antennas) and the diameter of the DSN antenna dish. The measurement's accuracy, characterized by the standard deviation of the Doppler post-fit residuals, is four times better for RISE (~1.1 mHz noise for data integrated over 60s) than Viking (~4.5 mHz@60s), see Extended Data Figure 1(a,b). The larger spread of the Viking residuals is mainly due to the medium contamination on the Viking S-band data.

Measurements preprocessing

The refraction of RISE radio waves traveling through Earth's troposphere and ionosphere, and, to a lesser extent, the Mars troposphere imparts a phase delay on the signal. The Earth atmosphere contribution is modeled using information provided by the DSN RadioMetric Data Conditioning (RMDC) Subsystem, in the form of TRK-2-23 files. These files include both seasonal and daily (second-order) calibrations, expressed as polynomials modeling the Earth troposphere and ionosphere delay at the zenith. The troposphere delay ($\Delta\rho$) is modeled as:

$$\Delta\rho = M_{dry}(d_o + d_b + d_p) + M_{wet}(w_o + w_b + w_p),$$

where d_o is the zenith dry offset, d_b is the zenith dry bias parameter, and d_p is a polynomial model of the zenith dry delay. Similarly, w_o is the zenith wet offset, w_b is the zenith wet bias parameter, and w_p is a polynomial model of the zenith wet delay. d_o , d_p , w_o , and w_p are models provided by the DSN media calibration system and given in the RISE archives (https://pds-geosciences.wustl.edu/insight/urn-nasa-pds-insight_rise_raw/data_tro/). M_{dry} and M_{wet} are respectively dry and wet Niell mapping functions³⁵ used to obtain the delay at specific elevations. The dry troposphere accounts for ~90% of the total media delay. The associated uncertainties are significantly smaller than for the wet part since these short-term variations are difficult to calibrate using GNSS data. This is why d_b is set to zero and w_b is estimated on a per-pass basis (details below). Daily calibrations for the ionosphere delay are an order of magnitude lower than those for the seasonal troposphere (Extended Data Figure 2a). Calibrations for the Mars' troposphere delay, performed following the method of Le Maistre (2020)³⁶, is indispensable for a reliable retrieval of the FCN parameters. At low elevations its contribution is close to that of the daily Earth troposphere corrections (Extended Data Figure 2a). The main source of inaccuracy in the Mars troposphere contribution predicted by the model results from the mapping function used. We tested both

‘flat’ and ‘geometric’ mapping functions presented in Le Maistre (2020)³⁶, which led us to conclude that the mapping function actually has little influence on the estimation of nutation parameters from RISE data.

Following the procedure of Buccino et al. (2022)³⁷, the raw TRK-2-34 tracking data, sampled at 0.1 sec by the DSN Block V Closed Loop Receiver, are compressed to 60 sec and then filtered based on the Sun-Earth-Probe (SEP) angle (or elongation) and the identification of outliers. ~2100 data points collected at SEP<15° (blue squares on Extended Data Figure 2b) are discarded because they are strongly affected by solar plasma noise. A wet troposphere bias parameter (w_b) is estimated for each pass with an a-priori uncertainty of 4 cm (Extended Data Figure 2c). The 1σ variation among each pass was approximately 5 cm. 86 passes larger than 1σ are removed, reducing the number of data points used from 25000 to 20500. 2700 additional measurements, with Doppler residuals larger than 3σ of the residuals (i.e. 3×1.1 mHz for RISE and 3×4.5 mHz for Viking 1 lander) are filtered out, leading to ~17000 points (or ~285 hours) of RISE tracking used in our solutions and ~11000 points (or ~185 hours) of Viking tracking. Removing outliers on a per-pass basis instead leads to ~1000 extra points for RISE and ~500 for Viking. This approach yields consistent Mars rotation and Orientation Parameters (MOP) estimates compared to the nominal settings, as long as these points are adequately deweighted based on the noise of the pass. Removal and weighting of the data on a per-mission rather than a per-pass basis was preferred due to the more conservative estimate uncertainties provided by the former.

Data analysis procedure

The 60-s Doppler measurements are analyzed using the Jet Propulsion Laboratory (JPL) Mission analysis, Operations and Navigation Toolkit Environment (MONTE) program⁷ and the Centre National d’Etudes Spatiales (CNES) Géodésie par Intégrations Numériques Simultanées (GINS) software^{8,9,38}. Both software packages are designed for orbital determination and trajectory optimization and analysis using an iterative least-squares procedure.

The Earth and Mars trajectories are obtained from the DE431 planetary ephemerides³⁹ but preliminary computations performed with DE440 led to MOP estimates compatible with our nominal solution at 1σ . Phobos and Deimos states are taken from the mar097 JPL ephemeris⁴⁰. DSN antenna positions are taken from global VLBI solutions. A model of rigid and ocean loading is introduced, and Earth plate tectonics is modeled with constant drifts based on GNSS, VLBI, SLR and DORIS observations. The Earth’s orientation parameters are provided by JPL’s Time and Earth Motion Precision Observation group for MONTE and the International Earth Rotation and Reference Systems Service (IERS) for GINS. Tidal deformations of the surface of Mars are accounted for using the conventional solid Earth tidal model^{41,42} (see IERS conventions). This generates variations in the 3D position of the lander of only a few millimeters in amplitude (10-100x smaller than displacement due to the liquid core). Deformations due to Mars atmospheric loading have been ignored.

Rotation models for celestial bodies are implemented differently in both software. GINS uses rotational elements with respect to the International Celestial Reference Frame (ICRF), i.e. the right ascension, α , and declination, δ , angles to position the pole of Mars with respect to

the Earth equator of epoch (J2000), and the rotation angle W to locate the prime meridian⁴³ (Extended Data Figure 3a). Five elementary rotations are needed to transform the lander position vector r_{icrf} expressed in the coordinates of the ICRF into the coordinates of a Mars body-fixed reference frame (r_{bf}):

$$r_{bf} = R_y(-X_p)R_x(-Y_p)R_z(W)R_x\left(\frac{\pi}{2} - \delta\right)R_z\left(\frac{\pi}{2} + \alpha\right)r_{icrf}. \#(M1)$$

MONTE uses Euler angles to describe Mars rotation, following the formulation of Konopliv et al. (2006)⁴⁴ (Extended Data Figure 3a):

- $I = I_0 + \dot{I}(t - t_0) + \Delta I$ is the inclination (obliquity) of the Mars true equator of date with respect to the Mars mean orbital plane at epoch,
- the longitude $\psi = \psi_0 + \dot{\psi}(t - t_0) + \Delta\psi$ locates the node C between those two planes and is measured from the node A .
- The spin angle $\phi = \phi_0 + \dot{\phi}(t - t_0) + \Delta\phi - \Delta\psi \cos I_0$ gives the position of the prime meridian of Mars and is measured along the true equator of date starting from the node C .

The Δ quantities are series of variations at harmonics of Mars orbital period (such series also exist for the α , δ , W angles). The transformation between r_{icrf} and r_{bf} is performed using seven elementary rotations:

$$r_{bf} = R_y(-X_p)R_x(-Y_p)R_z(\phi)R_x(I)R_z(\psi)R_x(J)R_z(N)r_{icrf}. \#(M2)$$

The longitude N and inclination J orientate the Mars mean orbit of epoch with respect to the ICRF. (X_p, Y_p) are the components of polar motion taken from Konopliv et al. (2020)¹⁰ in our a priori model. They are not estimated because of lacking sensitivity of the low-latitude InSight mission to such small signals⁹. Adding future mission radio-science data from higher latitudes would help to disentangle these parameters from the rest of the parameter set⁴⁵.

We compute pre-fit Doppler residuals to visualize the quality of our a priori model and the potential of the new data to improve the model. None of the a priori models of Konopliv et al. (2020)¹⁰ and Kahan et al. (2021)³³ flatten the residuals (Extended Data Figure 1c), revealing their limitation if we assume the errors in the non-rotation parameters are much smaller than the errors in the rotation parameters, as we think it is the case. Note that the numerical value reported in Kahan et al. (2021)³³ for the rotation rate (i.e. 350.8919825°/d) is actually \dot{W} . The corresponding value for $\dot{\phi}$ is 350.891985377°/d.

30-months dataset solution (full-arc)

Instead of determining the amplitudes of nutation (P', R' in Eq.1 of the main paper), we estimated the F and $\tau_{FCN} = 2\pi/\omega_{FCN}$ parameters of the nutation transfer function T_F (see Eq.2 of the main paper and Supplementary Section 4). Since the estimates of τ_{FCN} , F and $\dot{\psi}$ are not stable versus time (Extended Data Figure 4) with the “classical rotation model”⁴⁴, we extended that model and will refer to it as the “post-dust-storm model”.

With respect to the classical model, we add to the new model quadratic terms in the parametrization of the longitude and obliquity angles, as predicted by the precession/nutation theory¹¹. We also add terms at periods related to Phobos and Deimos motion for the obliquity and longitude angles. We keep the spin periodic series $\Delta\phi$ of the classical model, with terms from the annual to the quarter-annual periods^{33,44}:

$$\Delta\phi = \sum_{j=1}^4 (\phi_{c_j} \cos(jM) + \phi_{s_j} \sin(jM)), \#(M3)$$

where M is the mean anomaly and the sine amplitudes are corrected for relativistic effects according to Baland et al. (2023)⁴⁶. An extra set of annual amplitudes (ϕ'_{c1}, ϕ'_{s1}) is used to fit the slope observed in the early part of the mission (Extended Data Figure 1d). This slope in the residuals could be due to the decay of the global dust storm that occurred a few months before the InSight landing. The noticeably lower InSight pressure than those of Viking at similar solar longitudes⁴⁷ in the first 100-200 days of data is evidence of a global dust storm that perturbed the CO₂ cycle and resulted in a large deposition of ice at the Northern polar cap, which lasted longer than usual after the storm⁴⁸. This accumulation of CO₂ ice at the polar caps temporarily sped up the planet's rotation. Our estimates for those annual amplitudes represent a monotonically decreasing contribution to the spin angle over the first ~150 days of the RISE mission, which might actually characterize the temporary post-dust-storm deceleration in the rotation of Mars.

Since separate analyses of Viking and RISE data lead to incompatible estimates of the rotation rate and of the amplitudes of the periodic variations, we estimate in the global inversion separate sets of seasonal spin series for each era, along with a quadratic term ($\ddot{\phi}$) modelling a spin acceleration. The estimated amplitudes for each era are also quite different from previously published solutions^{10,33,49} and from the current IAU standard model⁴³. The latter model is driven by Viking data. The reason for the difference between the spin angle variations for the two eras is still under investigation but is likely related to the poor quality of Viking data.

The final adopted rotation model is given by

$$\begin{aligned} \psi(t) &= \psi_0 + \dot{\psi}(t - t_0) + \ddot{\psi}(t - t_0)^2 + \Delta\psi, \\ I(t) &= I_0 + \dot{I}(t - t_0) + \ddot{I}(t - t_0)^2 + \Delta I, \\ \phi(t) &= \phi_0 + \dot{\phi}(t - t_0) + \ddot{\phi}(t - t_0)^2 + \Delta\phi - \Delta\psi \cos I_0 + \Delta\phi_{DUST}, \end{aligned} \quad (M4)$$

where $\Delta\psi, \Delta I$ are the nutation series and $\Delta\phi$ is the spin series defined in Eq.M3 with amplitudes estimated separately for Viking and RISE eras. $\Delta\phi_{DUST} = \delta\phi_{c1} \cos(M) + \delta\phi_{s1} \sin(M)$ for the first 150 days of RISE data and 0 elsewhere, with $\delta\phi_{c1} = \phi'_{c1} - \phi_{c1}$ and $\delta\phi_{s1} = \phi'_{s1} - \phi_{s1}$ the ‘‘dust parameters’’. With the post dust-storm rotation model (Eq.M4), our FCN solution is equal to -242.8 +/- 3.8 days for MONTE and -243.0 +/- 2.7 days for GINS when the full set of selected data is used. The 30-months core amplification factor solutions for both software are in very good agreement with each other as well (see full arc solutions in Supplementary Table S1). F is more sensitive to the radius of the core than τ_{FCN} , which is mostly affected by its shape. The recent seismic data provided by InSight's SEIS experiment constrained the core radius to 1830 +/- 40 km¹⁷. This corresponds to a core factor ranging between 0.055 and 0.065 (see Fig. 2b of the main paper), which is in very good agreement with the RISE solution of $F = 0.0615 +/- 0.007$.

To ensure that Viking noisy data do not pollute our estimates, a pure RISE nutation solution has also been computed. Because it is impossible to decorrelate rates and angles at Epoch with RISE data only, we made different runs fixing the t_0 angles to different values (those of the present paper or those of Konopliv et al. (2020)¹⁰ and/or fixing the quadratic term to zero

($\ddot{\phi} = 0$) or to our nominal estimate). The so-obtained nutation parameter estimates remain consistent with our nominal solution (within our 1σ envelope), showing the negligible contribution of Viking to our nutation solution.

Our estimated precession rate $\dot{\psi} = -7,598.1 \pm 2.2$ mas/year (Fig. 1b of the main paper) is less than 3σ smaller than previous estimates obtained from lander data³³ and about 4σ smaller than the last orbiting spacecraft solution¹⁰. The difference with Kahan et al. (2021)³³ results from the longer RISE data coverage, from the change in our rotation rate estimate (now corrected for the observed secular acceleration), and from looser a priori constraints on the values of the angles at J2000 epoch, ψ_0 and I_0 , which are highly correlated with precession ($\dot{\psi}$) and obliquity (\dot{I}) rates (see a priori constraints in Supplementary Table S1 and correlation matrix in Extended Data Figure 3b).

Interior structure models

The core amplification factor F and the FCN period strongly depend on the state and shape of the core, on the principal moments of inertia of the core and mantle, and on the mantle's ability to deform. We construct our models in a two-step process: We first build spherical symmetric models (detailed below) that are in a second step deformed by the effect of rotation and internal loading (Supplementary Section 10).

We assume a spherically symmetric, three-layer interior structure model made of a crust overlying a solid mantle and liquid core. For each considered crustal structure, mantle composition and temperature, and core temperature profile, we compute a whole planet model following¹⁸. The free parameters are the core radius and the correlated values of the crustal thickness and density (Supplementary Section 8). The amount of light elements is set such that the models match the observed mass of Mars and only models agreeing with the MOI (moment of inertia) are retained. Since the FCN period depends on the moment of inertia of the core through its density, only combinations of light elements can be constrained. We use two mantle compositions models that roughly delineate the spread in mantle densities expected from published mantle models: the model of Yoshizaki and McDonough (2020)¹⁴ (denoted as YMD) and the EH45 model of Sanloup et al. (1999)¹³. The FeO content of the YMD model is low in comparison to that of the EH45 model and of other published compositions^{e.g.50}. We calculate the equilibrium mineralogy and phase proportions in the mantle as well as its density and elastic properties with the Gibbs energy minimization software *Perple_X*⁵¹ according the thermodynamic formulation and database of Stixrude et al. (2005)⁵² and considering two end-member temperature profiles (denoted as T_{hot} and T_{cold}) deduced from 3D thermal evolution studies of Mars (Supplementary Section 7).

The present thermal state of the liquid core depends mainly on the not well-known heat flow at the core mantle-boundary and on the thermal conductivity of the core material. The core temperature profile is likely subadiabatic, between that of an isotherm and the adiabat, in agreement with the absence of a present-day core dynamo^{e.g.53}. We assume that the fully liquid metallic core is either convecting or isothermal.

A large amount of light elements is required to match the core density^{e.g.17,18,54}, implying a core liquidus significantly lower than any plausible estimate of the present-day temperature in the Martian core. As such, the presence of an inner core is highly unlikely, although the

presence of remelting iron-rich snow in the core cannot be excluded (but neglected in our modeling). Formation conditions and geochemical models indicate that sulfur (S) is the main light element in the core together with smaller amounts of oxygen (O), carbon (C), and hydrogen (H)^{e.g.14,25,27,28}. We model the core as an Fe-O-S-C-H alloy (Supplementary Section 6). The abundances of the different light elements are not independent from each other. The correlation between the amount of S and O is described by a multi-stage core formation model²⁶. The correlation with the other light elements is not well known and neglected here. The amount of C is set to its saturation limit^{e.g.55} at core-mantle boundary conditions. The solubility of H in liquid Fe at the conditions of formation of the Martian core is highly controversial. It is difficult to constrain the abundance of H in the Martian core, with published results ranging between 60 ppm and 1.8wt%^{27,56,57,58,59}. Instead, we consider the H content of the core as a free parameter and determine its amount such that the core density agrees with the findings in this study and with cosmochemical constraints about the permissible amounts of S in the core.

The equations of state for the liquid core used in this study (Supplementary Section 6) are significantly improved with respect to those used in Stähler et al. (2021)¹⁷. The Fe-S system equation of state is based on a much larger set of experimental results, while the inclusion of the non-ideal mixing behavior of the Fe-FeS and Fe-FeO binaries is taken into account. Neglecting non-ideality in Fe-FeS can result in underestimating the fraction of S in the core by almost 4wt% and overestimating the amount of O in Fe-FeO by almost 1wt%.

The non-elastic behavior of the mantle and crust is described by a frequency-dependent but depth-independent model of shear dissipation^{e.g.60}. The parameters of the complex shear modulus are chosen so that the semi-diurnal tidal Love number k_2 , the period of the Chandler Wobble, and the secular acceleration of Phobos agree with observations (see Tab. S6 in Konopliv et al. (2020)¹⁰).

The compliances required for the calculation of F and FCN period (see equations main text) (Supplementary Section 9) are calculated from the spherical models following Dehant and Mathews (2015)³.

Data availability

The data that support the findings of this study are available on the Planetary Data system at <https://pds-geosciences.wustl.edu/missions/insight/rise.html>

ASCII versions of the Doppler data for Viking are in the REDUCED directories at <https://pds-geosciences.wustl.edu/missions/mpf/radioscience.html>

DSN media calibration files are given in the RISE PDS archives: https://pds-geosciences.wustl.edu/insight/urn-nasa-pds-insight_rise_raw/data_tro/

The full correlation matrix is available as source data for Extended Data Figure 3b.

Code availability

Distribution of the MONTE navigation code is restricted by the Export Administration Regulations of the US Department of Commerce. Eligible readers may request a copy of MONTE, under a license which does not permit redistribution, at <https://montepy.jpl.nasa.gov/>. GINS software is the property of CNES. It can only be used for

research; any other commercial or non-commercial uses are strictly prohibited. CNES grants to the GINS Licensee (natural person) a free non-exclusive license.

References from Methods

33. Kahan, D. *et al.*, Mars precession rate determined from radiometric tracking of the InSight lander. *Planet. Space Sci.* **199**, 105208 (2021).
34. Yseboodt, M., Dehant, V., Péters, M.-J., Signatures of the Martian rotation parameters in the Doppler and range observables. *Planet. Space Sci.* **144**, 74–88 (2017).
35. Estefan, J.A., and Sovers, O.J., JPL Publication **94-24** (1994)
36. Le Maistre, S., Martian Lander Radio Science Data Calibration for Mars Troposphere. *Radio Science*, **55**(12), 1–16 (2020).
37. D. Buccino, Border, J.S., Folkner, W. M., Kahan, K., Le Maistre, S., Low-SNR Doppler Data Processing for the InSight Radio Science Experiment. *Remote Sensing*. **14**(8), 1924 (2022).
38. Le Maistre, S., Rosenblatt, P., Dehant, V., Marty, J.-C., Yseboodt, M., Mars rotation determination from a moving rover using Doppler tracking data: What could be done? *Planet. Space Sci.* **159**, 17-27 (2018).
39. Folkner, W. M., Williams, J. G., Boggs, D. H., Park, R. S., Kuchynka, P., The planetary and lunar ephemerides DE430 and DE431, *Interplanetary Network Progress Rep.* **42**, 196 (2014).
40. Jacobson, R. A., Lainey, V., Martian satellite orbits and ephemerides. *Planetary and Space Science*. **102**, 35-44 (2014).
41. Dehant, V., Defraigne, P., and Van Hoolst, T., Computation of Mars' transfer functions for nutations, tides and surface loading. *Physics of the Earth and Planetary Interiors*, **117**, 385–395, January 2000.
42. Van Hoolst, T., Dehant, V., Roosbeek, F., and Lognonné, P., Tidally induced surface displacements, external potential variations, and gravity variations on Mars. *Icarus*, **161**, 281–296, 2 2003.
43. Archinal, B. A. *et al.*, Report of the IAU Working Group on Cartographic Coordinates and Rotational Elements: 2015. *Celestial Mech. Dyn. Astron.* **130**, 22 (2018).
44. Konopliv, A.S., Yoder, C.F., Standish, E.M., Yuan, D.-N., Sjogren, W.L., A global solution for the Mars static and seasonal gravity, Mars orientation, Phobos and Deimos masses, and Mars ephemeris. *Icarus* **182**(1), 23–50 (2006).
45. Dehant, V. *et al.*, The radioscience LaRa instrument onboard ExoMars 2020 to investigate the rotation and interior of Mars. *Planetary and Space Science*, **180**, 104776 (2020).
46. Baland, R.-M., Hees, A., Yseboodt, M., Bourgoïn, A., Le Maistre, S., Relativistic contributions to the rotation of Mars. *Astronomy and Astrophysics*, **670**:A29, *Astronomy and Astrophysics* (2023).

47. Lange, L. *et al.*, Insight pressure data recalibration, and its application to the study of long-term pressure changes on mars. *J. Geophys. Res., Planets* **127** (2022).
48. de la Torre, J.M., Piqueux, S., Kass, D.M., Newman, C., Guzewich, S.D., Pressure Deficit in Gale Crater and a Larger Northern Polar Cap after the Mars Year 34 Global Dust Storm. In *AGU Fall Meeting Abstracts*, **2019**, P51C-02 (2019).
49. Kuchynka, P. *et al.*, New constraints on Mars rotation determined from radiometric tracking of the opportunity Mars exploration rover. *Icarus* **229**, 340–347 (2014).
50. Panning, M. P. *et al.*, Planned products of the Mars structure service for the InSight mission to Mars. *Space Sci. Rev.* **211**, 611–650 (2016).
51. D.Connolly, J. A., Computation of phase equilibria by linear programming: a tool for geodynamic modeling and its application to subduction zone decarbonation. *Earth Planet. Sci. Lett.* **236**, 524–541 (2005).
52. Stixrude, L., Lithgow-Bertelloni, C., Thermodynamics of mantle minerals. Part 1: Physical properties. *Geophys. J. Int.* **162**, 610–632 (2005).
53. Greenwood, S., Davies, C.J., Pommier, A., Influence of Thermal Stratification on the Structure and Evolution of the Martian Core. *Geophysical Research Letters*, **48**(22), e2021GL095198 (2021).
54. Terasaki, H. *et al.*, Pressure and Composition Effects on Sound Velocity and Density of Core-Forming Liquids: Implication to Core Compositions of Terrestrial Planets. *J. Geophys. Res. Planets* **124**, 2272–2293 (2019).
55. Tsuno, K., Grewal, D. S., Dasgupta, R., Core-mantle fractionation of carbon in Earth and Mars: The effects of sulfur. *Geochim. Cosmochim. Acta* **238**, 477–495 (2018).
56. Okuchi, T., Hydrogen partitioning into molten iron at high pressure: implications for Earth's core. *Science* **278**, 1781–1784 (1997).
57. Clesi, V. *et al.*, Low hydrogen contents in the cores of terrestrial planets. *Sci. Adv.* **4**, e1701876 (2018).
58. Malavergne, V. *et al.*, Experimental constraints on the fate of H and C during planetary core-mantle differentiation. Implications for the Earth. *Icarus* **321**, 473–485 (2019).
59. Yuan, L., Steinle-Neumann, G., Strong sequestration of hydrogen into the Earth's core during planetary differentiation. *Geophys. Res. Lett.* **47**, e2020GL088303 (2020).
60. Anderson, D.L., Minster, J.B., The frequency dependence of Q in the Earth and implications for mantle rheology and Chandler wobble. *Geophys. J. R. Astron. Soc.* **58**, 431–440 (1979).

Acknowledgements

This is InSight Contribution Number 211.

Author contributions

Writing original draft: SLM, AR, MB, AC, MY, RMB, MD, HS. Writing review & editing: TVH, MW, DA. Formal Analysis: SLM, AC. Validation: DB, AK, MJP. Software: JCM, SLM, AC. Data curation: DK, DB, SLM, AC. Methodology: AR, MY, RMB, MB, TVH, DA, JB, MD, ACP, HS, NT. Investigation: SLM, AR, WMF, DK, DB. Conceptualization: WMF, VD, PL. Project administration: WBB, SS, MP.

Funding

This research carried out at the Royal Observatory of Belgium was financially supported by the Belgian PRODEX program managed by the European Space Agency in collaboration with the Belgian Federal Science Policy Office under contract number PEA4000129361; The work of AC was financed by the French Community of Belgium within the frame of a FRIA grant. Part of the work was performed at the Jet Propulsion Laboratory, California Institute of Technology, under contract with the National Aeronautics and Space Administration. French co-authors acknowledge support from CNES and ANR (ANR-19-CE31-0008-08) and JB, HS and PL from *IdEx Université de Paris (ANR-18-IDEX-0001)*. DA has received funding from the European Research Council (ERC) under the European Union's Horizon 2020 research and innovation Programme (Grant agreement 724690). The computation of BSL models was granted access to the HPC resources of IDRIS under the allocation A011041317 made by GENCI. JB acknowledges support from the European Research Council under the European Union's Horizon 2020 research and innovation program (grant agreement no. 101019965—ERC advanced grant SEPTiM).

Competing interests

The authors declare no competing interests.

Additional information

Supplementary information is available for this paper.

Extended Data Figure/Table legends

Extended Data Table 1: 2-way Doppler data at 60 s of integration time considered in this study.

Extended Data Table 2: Best solution of the main Mars rotation parameter estimates corresponding to an average of the GINS and MONTE sets of full arc solutions reported in

Supplementary Table S1. Uncertainties are $\sigma = \sqrt{\frac{\sigma_M^2 + \sigma_G^2 + (p_M - p_G)^2}{2}}$, where $p_M \pm \sigma_M$ and $p_G \pm \sigma_G$ are MONTE and GINS solutions (central value plus or minus formal errors), respectively.

Extended Data Figure 1: RISE Doppler residuals and signature of the liquid core. Post-fit Doppler residuals and their histogram distributions for RISE **(a)** and Viking 1 lander **(b)** as a function of the mission time after landing and of the DSN facilities location. **(c)** Pre-fit Doppler residuals of RISE data as a function of time computed with the latest rotation models of Konopliv et al. (2020)¹⁰ (in blue) and Kahan et al. (2021)³³ (in orange). **(d)** Pre-fit residuals with nominal values of the classical rotation model parameters coming from converged RISE solution using only the first 24 months of data (blue) and only the last 24 months of data (orange). This shows that the classical model fails at matching RISE full arc data since a clear trend is observed in the regions not covered by the corresponding nominal solution. **(e)** Theoretical signature of the liquid core for the RISE timing, separated in red for the East antenna and in green for the West antenna tracking. The FCN parameters are $F = 0.06$ and FCN period of -243 days. The orange envelope shows the signature when the FCN period is slightly different (between -238 and -248 days). The pink box is the interval where the SEP angle is smaller than 15° (conjunction) while the grey boxes are the intervals where the Earth declination is close to 0° . The signature of a parameter in the Doppler observable is the difference between the observable computed using a nominal/non-zero value for this parameter and that obtained when the parameter is set to 0³⁴.

Extended Data Figure 2: RISE data calibrations. **(a)** Correction for media delays as applied to the RISE data points. On the left, the corrections due to the Earth's atmosphere as a function of the elevation at the DSN, on the right those due to Mars' troposphere, as a function of their elevation at Mars. **(b)** RISE Doppler residuals: only the red points are processed, i.e. used in our analysis. Points acquired at low elevation above the DSN station (orange diamonds) are affected by significant noise from the Earth's atmosphere. They are still part of our analysis thanks to our accurate Earth noise calibration. The rest of the points are eliminated due to low SEP (blue squares), or high residual value (green crosses). **(c)** Estimated wet troposphere bias parameter per pass, classified by DSN station identifier. Shaded area is the a priori uncertainty.

Extended Data Figure 3: Mars rotation and orientation angles and their correlations. **(a)** Reference frames and Mars orientation angles (orange and green) for conversion between the Earth mean equator of J2000 (in blue) and Mars body-fixed coordinates (in red). **(b)** Correlation matrix between MONTE solved parameters (GINS correlation matrix is equivalent) using the full set of RISE data (see Supplementary Table S1 for symbol definition). Values smaller than 0.3 are set to 0 for readability.

Extended Data Figure 4: Comparison between the classical model of rotation of Mars and the one proposed in this study. Temporal evolution of the 30-months solutions for the FCN period **(a)**, the core amplification factor **(b)**, and the precession rate **(c)**, with the classical spin model (orange) and with the model with corrections on the rotation rate for the post-dust-storm period (blue). Shaded envelopes are 1σ uncertainty bounds.

Spin state and deep interior structure of Mars from InSight radio tracking

Authors: Sébastien Le Maistre^{1,2*}, Attilio Rivoldini¹, Alfonso Caldiero^{1,2}, Marie Yseboodt¹, Rose-Marie Baland¹, Mikael Beuthe¹, Tim Van Hoolst^{1,3}, Véronique Dehant^{1,2}, William M. Folkner⁴, Dustin Buccino⁴, Daniel Kahan⁴, Jean-Charles Marty⁵, Daniele Antonangeli⁶, James Badro⁷, Mélanie Drilleau⁸, Alex Konopliv⁴, Marie-Julie Péters¹, Ana-Catalina Plesa⁹, Henri Samuel⁷, Nicola Tosi⁹, Mark Wieczorek¹⁰, Philippe Lognonné⁷, Mark Panning⁴, Suzanne Smrekar⁴, W. Bruce Banerdt⁴.

Supplementary Discussion	2
Section 1. GINS-MONTE cross-validation	2
Section 2. A priori value of FCN period	2
Section 3. Inner core signature	3
Section 4. Full set of estimated parameters	4
Section 5. Principal moments of inertia	11
Section 6. Equation of state for the liquid core	11
Section 7. Thermal state of the mantle	12
Section 8. Crustal structure	14
Section 9. Anelasticity, triaxiality, CMB coupling, and Chandler wobble	14
Section 10. Core shape of non-hydrostatic planet	15
Section 11. Enriched basal silicate layer (BSL)	17
Section 12. Core structure and composition	19
Section 13. Shape and moment of inertia of the core	21
Supplementary references	23

Supplementary Discussion

Section 1. GINS-MONTE cross-validation

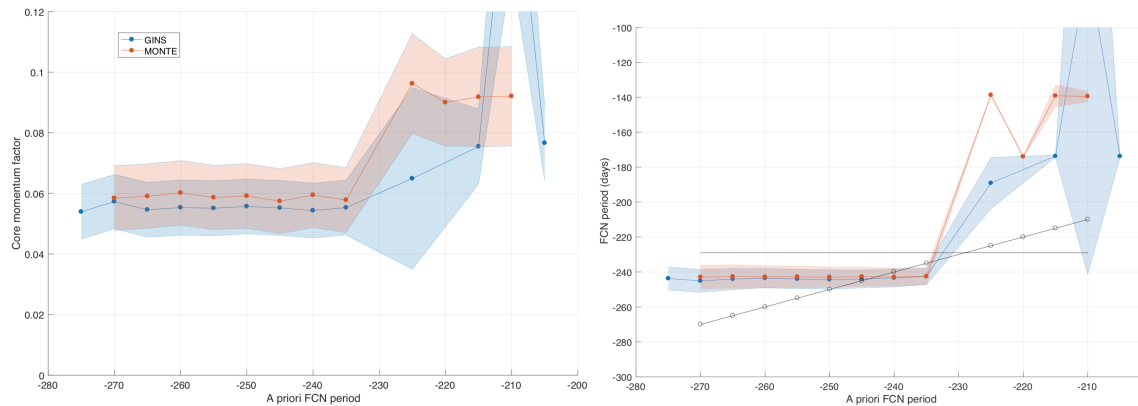
When using consistent a priori settings, the components of the rotation matrices of MONTE and GINS, positioning the axes of the Mars body-fixed frame, differ by 10^{-9} . This corresponds to a rotation of about 0.5 mas (milliarcseconds) in an angle-axis representation. MONTE, contrary to GINS, is not able in its present state to include the nutation terms induced by Phobos and Deimos (10 and 4 mas amplitude¹¹) in the rotation model. Therefore the rotation matrices comparison between both software has been performed without these nutation terms, which are taken into account for the inversion of RISE data with GINS*.

The relative difference in partial derivatives computed by each software is below $\sim 0.5\%$ for both the F factor and FCN frequency. The difference in theoretical Doppler measurements computed by GINS and MONTE with consistent settings is of the order of 0.1 mHz, 10 times smaller than the noise and significantly smaller than the signature of the liquid core ($\sim 0.4\text{mHz}$, Extended Data Figure 1e).

Section 2. A priori value of FCN period

The FCN period parameter, τ_{FCN} , appears in a nonlinear way in the equations (see Eq.2 main paper). This makes the Doppler derivative dependent on the a priori value of τ_{FCN} , which therefore influences the solution. To circumvent the possible hazard of having our τ_{FCN} estimate falling into a local minimum, we adopted an iterative approach where the partial derivative of the MOPs, and especially those of τ_{FCN} , are computed at each iteration using the numerical values estimated in the previous iteration. Several runs are carried out, each time starting from a different a priori value of τ_{FCN} for iteration 1 taken every 5 days within the range of -275 days to -205 days. Such a range is expected to cover all possible FCN periods for Mars as predicted by interior models^{e.g.,2,45}.

Supplementary Figure S1 clearly shows that when the a priori value of the FCN period is smaller than the ter-annual period (~ -229 days), the fitted core amplification factor and FCN period converge, while for an FCN a priori value larger than the ter-annual period, there is no convergence.



Supplementary Figure S1: Estimated core amplification factor (left) and FCN period (right) as a function of the a priori value of the FCN period, for GINS and MONTE, using 24-months of RISE data (Prime mission).

The horizontal line in the graph on the right panel corresponds to the ter-annual period where there can be a resonance. The equation of the black dotted line on the right panel is $y=x$. It corresponds to the starting a priori value of τ_{FCN} . Shaded envelopes are 1σ uncertainty bounds.

* Note that nutations induced by Phobos and Deimos have negligible impact on the FCN estimate.

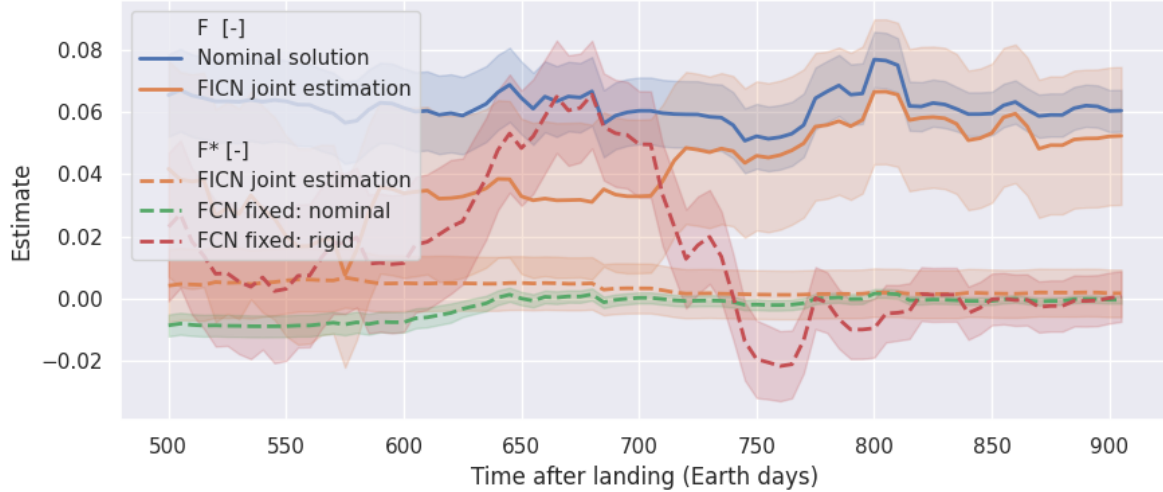
Section 3. Inner core signature

For the present-day thermal state of Mars, the iron alloy of the core can only crystallize and form an inner core if the sulfur weight fraction is below 3wt%. Mass conservation then implies that the core radius must be smaller than about 1400 km, which is not in agreement with the core amplification factor F determined in this study and with estimates deduced from tides¹⁸ and from core reflected shear waves¹⁷. Interior structure models that agree with the findings of this study require a large fraction of light elements (see Fig. 4 of the main paper) and consequently the core temperature must be significantly below any plausible present-day estimate for an inner core to be possible (Supp: Core structure and composition). The transfer function we use in the main paper (see Eq.2) therefore applies to the case of a fully liquid core and is expressed in terms of a resonance with the Free Core Nutation. If, despite what just preceded, Mars has a solid inner core, the transfer function would depend on an additional nutational normal mode, the Free Inner Core Nutation (FICN)³. Similarly to the FCN mode, which represents a relative motion of the liquid (part of the) core with respect to the mantle, the FICN describes a relative rotation of the inner core with respect to the outer core and mantle. Contrary to the FCN, which results in a retrograde motion of the rotation axis in space ($\omega_{FCN} < 0$), the FICN (also referred to as the Prograde Free Core Nutation or PFCN) has a prograde frequency ($\omega_{FICN} > 0$). We here show that the inclusion of an inner core in the transfer function does not significantly affect the estimation of the F factor and the FCN period and that the resonance strength of the FICN resonance is consistent with zero.

The transfer function that takes into account an inner core can be expressed as

$$T_F(\omega) = 1 + F \frac{\omega}{\omega - \omega_{FCN}} + F^* \frac{\omega}{\omega - \omega_{FICN}}, \quad (S1)$$

where ω_{FICN} is the unknown FICN prograde frequency, and F^* the FICN resonance strength. A preliminary analysis with transfer function (Eq.(S1)) did not allow us to reliably estimate the four transfer function parameters simultaneously. This is mainly because the $\tau_{FICN} = 2\pi/\omega_{FICN}$ estimate is strongly driven by its a priori value and never properly converges, whatever the a priori value taken between 200 and 575 days³⁰. Therefore, we only fitted ω_{FCN} , F and F^* along with the other MOPs and position parameters, for a range of chosen values for ω_{FICN} . We get $F = 0.052 \pm 0.022$ (see solid orange curve in Supplementary Figure S2) and $\tau_{FCN} = -242.5 \pm 11$ days. Both values are within the 1σ intervals of the results for an entirely liquid core (see Supplementary Table S1 and Extended Data Table 2), but affected by error bars ~ 4 times larger. The results for F and τ_{FCN} are therefore not significantly affected by the simultaneous estimation of F^* and the value set for ω_{FICN} . Our F^* estimate is always consistent with zero at 1σ and the average solution is $\bar{F}^* = 4.10^{-5} \pm 0.007$. Supplementary Figure S2 dashed curves show the temporal evolution of our F^* estimate for different scenarios of fit (see details in the caption of the figure). The uncertainty bound of F^* in the joint estimation case has been calibrated to account for the variability of the solutions as a function of the FICN period. We conclude from this analysis that $F^* \simeq 0$, indicating that no signature of an inner core is observed in the data and that the use of Eq.2 (main paper) for T_F is justified.



Supplementary Figure S2: Temporal evolution of preliminary estimates of F^* (dashed curves) assuming no FCN contribution (i.e. $F = 0$ in Eq.(S1)) for the “rigid” case or assuming $F = 0.06$ and $\tau_{FCN} = -243$ days for the “nominal” case. Orange solutions are obtained from a joint estimation of τ_{FCN} , F (solid curve) and F^* (dashed curve) and with $\tau_{FCN} = 400$ days. Shaded envelopes are 1σ uncertainties expect for F^* uncertainty which is up-scaled to a conservative value $\sigma_{F^*} = 0.007$ that takes into account our lack of knowledge on τ_{FCN} . The nutation transfer function parameters are always fitted along with the full set of MOPs.

Section 4. Full set of estimated parameters

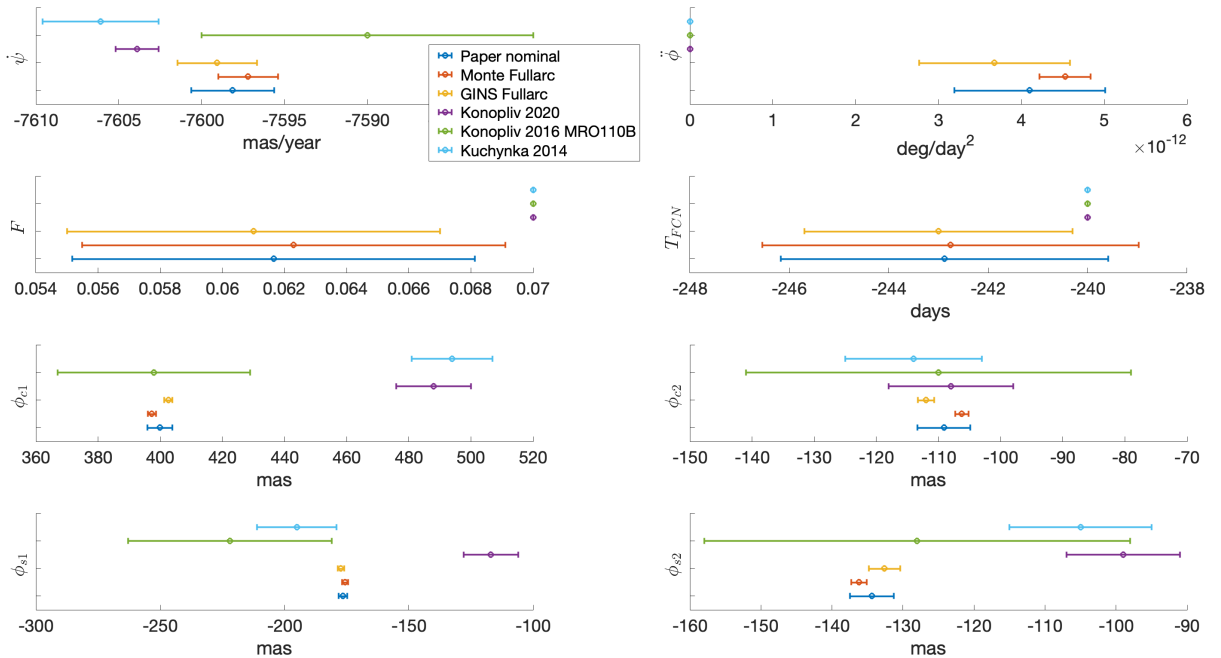
Our solutions using the 24-months Prime mission data and the full set of 30-months of data that have been pre-processed so far are reported in Supplementary Table S1, along with the a priori values of the parameters and the constraints. They have been obtained using GINS and MONTE independently. The Prime mission solutions are obtained with the classical rotation model, while the Full-arc solutions require the post-dust-storm model to stabilize the solutions (see Methods and Extended Data Figure 1d). Note that the quadratic terms added in the longitude and obliquity angles of the post-dust-storm model does not really help improving the solution stability. We expected the deficiency in the rotation model to come from the spin angle, for which variations are hard to predict: atmospheric phenomena (e.g. dust storms) can excite planet rotation variations in a broad frequency band, whereas the nutation frequencies are known from celestial mechanics. Therefore, we extensively tested improvements to the modelling of the spin angle that would help stabilize the solution. An extension of the spin series to harmonics up to order eight and the addition of a bi-annual term did not improve our estimates. The spin angle amplitudes at harmonics higher than order four were consistent with zero, meaning that order four is still adequate for RISE. We obtained a significant improvement in the stabilization of the nutation solution by fitting separately the first ~ 150 days of data and the remaining data as explained in Methods. As an alternative approach to the modeling of the slope in the residuals, we fitted two other extra parameters for the first 150d interval: a bias in the initial spin angle ($\delta\phi_0$) and one in the rotation rate ($\delta\dot{\phi}$). The latter is a correction to the global estimate of $\dot{\phi}$, itself obtained from the entire set of RISE and Viking combined. The corresponding MOP solution, not shown here, is consistent with that of the post-dust-storm model. Moreover, the estimates of $\delta\phi_0 \approx 6.3 \cdot 10^{-6} \pm 7.7 \cdot 10^{-7}$ deg and $\delta\dot{\phi} \approx -6.3 \cdot 10^{-8} \pm 6.5 \cdot 10^{-9}$ deg/day support the hypothesis of a deceleration of the planet in the early phase of the mission.

Full arc solutions are used to provide the preferred solutions, reported in Extended Data Table 2, which basically consists of the average of the GINS and MONTE sets of full arc solutions ($p = (p_M + p_G)/2$), with error bars computed as follows $\sigma = \sqrt{\frac{\sigma_M^2 + \sigma_G^2 + (p_M - p_G)^2}{2}}$, where $p_M \pm \sigma_M$ and $p_G \pm \sigma_G$ are MONTE and GINS solutions (central value plus or minus formal errors), respectively. Note that the corresponding lander positions and spin amplitudes at Viking era can also be retrieved by averaging GINS and MONTE full arc solutions.

The last column of Supplementary Table S1 provides the overlapping factor $\kappa = |p_M - p_G| / \sqrt{(\sigma_M^2 + \sigma_G^2)}$, by which the MONTE and GINS full-arc uncertainties need to be multiplied in order to overlap. Note that our geophysical interpretations and conclusions, based on our preferred solution of Extended Data Table 2, take full account of these GINS-MONTE differences. Note also that the overlapping factors are systematically lower than one when comparing our solutions with those of Folkner et al. (1997)⁵, meaning that our solutions are compliant at one sigma with the latter. It is worth mentioning that Folkner et al. (1997)⁵ fitted the MOP to the combined Viking and Mars Pathfinder data, but the very short Pathfinder life time (90 days) has a very small influence on the spin series amplitude estimates, which involve periods greater than 171 days (quarter-annual). Also worth mentioning is that both MONTE and GINS solutions have at least one large amplitude estimate (i.e. above 20 mas) for either the ter- or the quarter-annual wave or for both, which is difficult to explain/believe.

The difference between GINS and MONTE in the estimates of the equatorial coordinates of the lander's antennas (X and Y) is mainly due to the difference in the $\dot{\phi}$ estimates and to the shift in ϕ_0 for the GINS solutions, which is inherent in the conversion from α, δ, W to $I, \psi, \phi^{\delta 1}$.

Supplementary Figure S3 shows the compatibility of the Full-arc solutions of Supplementary Table S1 with the nominal solution of this paper (as reported in Extended Data Table 2) and with three recent solutions from the literature^{10,62,49}.



Supplementary Figure S3: Compatibility of our Full-arc solutions with recently published solutions^{10,62,49}. Error bars are 1σ uncertainties.

Parameter	Symbol	Unit	A priori value	A priori const	Value and Uncertainty				Overlapping factor between GINS and MONTE Full-arc
					GINS		MONTE		
					Prime mission (1 st dataset of 735d)	Full-arc (of 905 days)	Prime mission (1 st dataset of 735d)	Full-arc (of 905 days)	
Mars orbit inclination of 1980	J	deg	24.67682669	-	fixed	fixed	fixed	fixed	-
Longitude of Mars orbit ascending node of 1980	N	deg	3.37919183	-	fixed	fixed	fixed	fixed	-
Prime meridian at J2000 wrt Mars orbit at 1980	ϕ_0	deg	133.386373	-	133.38641351* ± 0.000012	133.38641504* ± 0.0000074	fixed	fixed	-
Longitude of node at J2000 wrt Mars orbit at 1980	ψ_0	deg	81.968392	0.0028	81.96836305 ± 0.000011	81.96836478 ± 0.0000104	81.96836513 ± 0.00001	81.96835322 ± 0.0000100	0.80
Precession rate at J2000 wrt Mars orbit at 1980	$\dot{\psi}$	mas/yr	-7603.9	100	-7598.235 \pm 2.4	-7599.057 \pm 2.4	-7599.170 \pm 1.9	-7597.195 \pm 1.80	0.62
Quadratic longitude coefficient	$\ddot{\psi}$	mas/yr ²	-0.0144	-	fixed	fixed	fixed	fixed	-
Obliquity at J2000 wrt Mars orbit at 1980	I_0	deg	25.189381	0.0028	25.18940990 ± 0.0000052	25.18941255 ± 0.0000047	25.18940909 ± 0.0000045	25.18940603 ± 0.0000044	1.00
Obliquity rate at J2000 wrt Mars orbit at 1980	\dot{I}	mas/yr	-1.2	100	-8.129 \pm 1	-8.682 \pm 1	-8.080 \pm 0.80	-7.301 \pm 0.79	1.08
Quadratic obliquity	\ddot{I}	mas/yr ²	0.0020	-	fixed	fixed	fixed	fixed	-

coefficient										
Rotation rate at J2000 wrt Mars orbit at 1980	$\dot{\phi}$	deg/day	350.891985314	-	$350.891985349438 \pm 0.000000013$	$350.891985346409 \pm 0.000000014$	$350.891985325764 \pm 0.0000000050$	$350.891985331763 \pm 0.0000000049$	0.99	
Rotation quadratic coefficient	$\ddot{\phi}$	deg/day ²	0	2e-10	$2.6078e-12 \pm 8.9e-13$	$3.7017e-12 \pm 9.1e-13$	$3.9741e-12 \pm 3.1e-13$	$4.5291e-12 \pm 3.1e-13$	0.86	
Core amplification factor	F	-	0.07	-	0.057 ± 0.009	0.061 ± 0.006	0.060 ± 0.011	0.062 ± 0.0068	0.14	
FCN period	τ_{FCN}	day	-240	-	-243.9 ± 5.1	-243.0 ± 2.7	-243.1 ± 5.5	-242.8 ± 3.8	0.05	
LOD variation amplitudes	Viking era	ϕ_{C1}	mas	488	100	549 ± 14	546 ± 15	525 ± 6	526 ± 6	1.26
		ϕ_{C2}	mas	-108	100	-65 ± 24	-71 ± 25	-112 ± 8	-108 ± 8	1.41
		ϕ_{C3}	mas	-16	100	9 ± 21	-1 ± 21	-41 ± 9	-36 ± 9	1.56
		ϕ_{C4}	mas	3	100	-51 ± 19	-42 ± 19	-34 ± 7	-34 ± 7	0.38
		ϕ_{S1}	mas	-117	100	-179 ± 28	-175 ± 28	-206 ± 11	-219 ± 11	1.48
		ϕ_{S2}	mas	-99	100	-29 ± 20	-35 ± 20	-69 ± 9	-74 ± 8	1.80
		ϕ_{S3}	mas	-9	100	-17 ± 24	-5 ± 24	28 ± 10	22 ± 10	1.04
		ϕ_{S4}	mas	-2	100	-21 ± 19	-18 ± 20	-3 ± 7	-5 ± 6	0.61
	InSight era	ϕ_{C1}	mas	488	100	414.2 ± 1.5	402.6 ± 1.3	415.0 ± 1.6	397.3 ± 1.3	2.89
		ϕ_{C2}	mas	-108	100	-111.5 ± 1.5	-112.0 ± 1.3	-109.3 ± 1.3	-106.2 ± 1.1	3.44
		ϕ_{C3}	mas	-16	100	-9.0 ± 1.2	-10.7 ± 0.8	-9.3 ± 1.0	-8.8 ± 0.8	1.69
		ϕ_{C4}	mas	3	100	-4.4 ± 0.9	-1.0 ± 0.7	-3.8 ± 1.0	1.7 ± 0.9	2.42
		ϕ_{S1}	mas	-117	100	-182.7 ± 1.7	-177.3 ± 1.3	-181.6 ± 1.3	-175.6 ± 1.2	0.93
		ϕ_{S2}	mas	-99	100	-128.8 ± 3.3	-132.6 ± 2.2	-132.1 ± 1.2	-136.2 ± 1.1	1.46

		ϕ_{S3}	mas	-9	100	-17.7 ± 1.8	-20.8 ± 1.4	-19.1 ± 0.7	-23.7 ± 0.6	1.88
		ϕ_{S4}	mas	-2	100	-11.0 ± 0.9	-11.9 ± 0.7	-12.1 ± 0.9	-11.5 ± 0.7	0.37
Dust parameter		$\delta\phi_{c1}$	mas	0	100	-	37 ± 4.9	-	28 ± 3	1.57
		$\delta\phi_{s1}$	mas	0	100	-	-20 ± 7.3	-	0.2 ± 2	2.67
Insight West antenna coordinates (body-fixed frame)		x_w	m	-2417532.54	1000	-2417505.9 ± 2	-2417504.5 ± 2	-2417511.8 ± 0.9	-2417508.9 ± 0.9	2.01
		y_w	m	2365926.6	1000	2365953.1 ± 2	2365954.5 ± 2	2365947.0 ± 0.9	2365950.0 ± 0.9	2.05
		z_w	m	266330.0	20	266248.9 ± 17	266266.7 ± 16	266307.3 ± 15	266338.3 ± 13.8	3.39
Insight East antenna coordinates (body-fixed frame)		x_e	m	-2417533.60	1000	-2417507.0 ± 2	-2417505.5 ± 2	-2417512.9 ± 0.9	-2417510.0 ± 0.9	2.05
		y_e	m	2365925.8	1000	2365952.2 ± 2	2365953.8 ± 2	2365946.2 ± 0.9	2365949.2 ± 0.9	2.10
		z_e	m	266330.0	20	266248.7 ± 17	266266.3 ± 16	266307.3 ± 15	266336.7 ± 14	3.31
Viking L1 antenna coordinates (body-fixed frame)		x_v	m	2100790.03	1000	2100724 ± 6	2100719 ± 7	2100714 ± 2	2100716 ± 2	0.41
		y_v	m	-2329042.25	1000	-2329101 ± 6	-2329105 ± 6	-2329110 ± 2	-2329109 ± 2	0.63
		z_v	m	1284466.76	20	1284397 ± 84	1284396 ± 88	1284436 ± 20	1284381 ± 20	0.17

Supplementary Table S1: Parameters estimates obtained using the first 24 months (~735d) of RISE data (Prime mission results) and the full set of 30 months of data (full arc results), systematically combined with the Viking 1 lander data. Uncertainties are 1σ formal errors. *Because GINS works in α, δ, W , the angle W_0 is fixed but ϕ_0 varies from one solution to another due to the difference in the α_0 and δ_0 estimates. Despite their level of uncertainty (i.e. significant digits), angles ($^\circ$), rates (mas/yr and $^\circ$ /d) and quadratic ($^\circ$ /d²) estimates are given with 8, 3, 12 and 16 digits respectively in order to ensure 0.1 mas precision in the angles conversion between (α, δ, W) and (ψ, I, ϕ) , even when computed 20 years away from J2000⁶¹.

The matrix of correlations of the main parameters is shown in Extended Data Figure 3b and the full correlation matrix provided as csv file (Source Data). From this figure, we see that F and the FCN period are significantly correlated with each other and with the spin angle amplitudes, especially F and ϕ_{s2} . Despite the long data span of Viking plus RISE combination, and the high accuracy of RISE data, we still observe high (anti) correlations between ψ_0 and $\dot{\psi}$ and between I_0 and \dot{I} . These correlations are primarily responsible for the difference in precession rate with respect to our result based on one Earth year only³³, which was obtained with stronger a priori constraints on the angles at J2000 (ψ_0, I_0). They also explain the difference with the orbiter estimate¹⁰ that we retrieve exactly by fixing (ψ_0, I_0) to Konopliv et al. (2020)¹⁰, with no significant impact on the nutation estimates. Moreover, the significant change in our $\dot{\phi}$ estimate with respect to Kahan et al. (2021)³³ indirectly affects the precession estimate since correlations between $\dot{\phi}$ and $\dot{\psi}$ are rather strong. This change of $\dot{\phi}$ of more than two times its error bars results from the estimation of a new parameter, $\ddot{\phi}$, which allowed us to model the accelerating rotation observed between Viking and RISE eras.

Following previous studies (see e.g. Fig. 18 of Konopliv et al. (2006)⁴⁴), we chose to describe the orientation of Mars with respect to the mean orbit of Mars of 1980 (see Supplementary Table S1). Considering Mars mean orbit of epoch J2000 instead, we would have $N = 3^\circ.37321423$ and $J = 24^\circ.67706841$ for the angles orienting the mean orbit with respect to ICRF. The prior values for Mars orientation angles would be $\phi_0 = 133^\circ.384992$ ($\dot{\phi} = 350.891985313422$ °/day), $I_0 = 25^\circ.191818$ ($\dot{I} = -1.28$ mas/yr), and $\psi_0 = 81^\circ.975074$ ($\dot{\psi} = -7603.21$ mas/yr). For the preferred solution: $\phi_0 = 133^\circ.3850127$ ($\dot{\phi} = 350.891985338504$ °/day), $I_0 = 25^\circ.19184671$ ($\dot{I} = -7.98$ mas/yr), and $\psi_0 = 81^\circ.97504061$ ($\dot{\psi} = -7597.41$ mas/yr).

As specified before, the GINS software works with α, δ, W angles, which are converted in I, ψ, ϕ in a post-processing phase of the analysis. The angles at epoch, rates, and periodic variations are converted using the geometrical relations between the two sets of angles that can be derived by equating Eqs. (M1) and (M2). Specifically, those relations take the following analytical form for the periodic variations in angles orienting the spin axis in space:

$$\Delta\psi = \Delta\alpha \frac{\cos J - \sin\delta\cos I_0}{\sin^2 I_0} + \Delta\delta \frac{\sin J \cos(\alpha_0 - N)}{\sin^2 I_0}, \quad (S2)$$

$$\Delta I = \Delta\alpha \frac{\cos \delta_0 \sin J \cos(\alpha_0 - N)}{\sin I_0} - \Delta\delta \frac{\cos \delta_0 \cos J + \sin \delta_0 \sin J \sin(\alpha_0 - N)}{\sin I_0}. \quad (S3)$$

Replacing the non- Δ quantities of the above equation by their numerical values, we get

$$\Delta\psi = 1.03258 \Delta\alpha + 1.60964 \Delta\delta, \quad (S4)$$

$$\Delta I = 0.41341 \Delta\alpha - 0.72841 \Delta\delta. \quad (S5)$$

The spin angle amplitudes are modeled in GINS according to the following formalism

$$\Delta W = \sum_{j=1}^4 (W_{cj} \cos(jnt) + W_{sj} \sin(jnt)), \quad (S6)$$

where n is the mean motion of Mars and t is the time past J2000. Reminding that $M = nt + M_0$, with the Mars mean anomaly at J2000 $M_0 = 19.35743065^\circ$, the above W_{cj}, W_{sj} amplitudes for the spin angle can be converted into ϕ_{cj}, ϕ_{sj} amplitudes of Eq.(M3) according to:

$$\phi_{cj} = (W_{cj} + \alpha_{cj} \sin\delta_0) \cos(jM_0) - (W_{sj} + \alpha_{sj} \sin\delta_0) \sin(jM_0), \quad (S7)$$

$$\phi_{sj} = (W_{sj} + \alpha_{sj} \sin\delta_0) \cos(jM_0) + (W_{cj} + \alpha_{cj} \sin\delta_0) \sin(jM_0) - \phi_{rj}, \quad (S8)$$

ϕ_{rj} are the relativistic periodic corrections due to variations in Mars orbit radius^{6,44} that we apply to our raw amplitude estimates to produce our ϕ_{cj}, ϕ_{sj} solutions reported in Supplementary Table S1. We use $\phi_{r1} = -166.95$ mas, $\phi_{r2} = -7.78$ mas and $\phi_{r3} = -0.54$ mas⁴⁶. The α_{cj}, α_{sj} amplitudes are the amplitudes of nutation computed from the rigid nutation ($\alpha_{cj}^r, \alpha_{sj}^r, \delta_{cj}^r, \delta_{sj}^r$) of Baland et al. (2020)¹¹ (see <https://doi.org/10.24414/h5pn-7n71>, last columns of bottom table at <https://lara.oma.be/RigidNutations/bman20rs.dat>) according to:

$$\alpha_{cj} = \alpha_{cj}^r \left(1 + F \frac{(jn)^2}{(jn)^2 - \omega_{FCN}^2} \right) + \delta_{sj}^r \cos^{-1}(\delta_0) \left(F \frac{jn\omega_{FCN}}{(jn)^2 - \omega_{FCN}^2} \right), \quad (S9)$$

$$\alpha_{sj} = \alpha_{sj}^r \left(1 + F \frac{(jn)^2}{(jn)^2 - \omega_{FCN}^2} \right) - \delta_{cj}^r \cos^{-1}(\delta_0) \left(F \frac{jn\omega_{FCN}}{(jn)^2 - \omega_{FCN}^2} \right), \quad (S10)$$

$$\delta_{cj} = \delta_{cj}^r \left(1 + F \frac{(jn)^2}{(jn)^2 - \omega_{FCN}^2} \right) - \alpha_{sj}^r \cos(\delta_0) \left(F \frac{jn\omega_{FCN}}{(jn)^2 - \omega_{FCN}^2} \right), \quad (S11)$$

$$\delta_{sj} = \delta_{sj}^r \left(1 + F \frac{(jn)^2}{(jn)^2 - \omega_{FCN}^2} \right) + \alpha_{cj}^r \cos(\delta_0) \left(F \frac{jn\omega_{FCN}}{(jn)^2 - \omega_{FCN}^2} \right). \quad (S12)$$

The GINS raw solutions in α , δ , W , equivalent to the Full-arc solution reported in Supplementary Table S1, are shown in Supplementary Table S2 below.

Parameter		Symbol	Unit	GINS
Right ascension at J2000		α_0	deg	$317.681132336 \pm 0.0000075$
Right ascension rate		$\dot{\alpha}$	mas/yr	-3914.253 ± 1.3
Quadratic right ascension coefficient		$\ddot{\alpha}$	mas/yr ²	-0.0108 (fixed)
Declination at J2000		δ_0	deg	$52.88632054 \pm 0.0000066$
Declination rate		$\dot{\delta}$	mas/yr	-2209.5470 ± 1.2
Quadratic declination coefficient		$\ddot{\delta}$	mas/yr ²	0.0159 (fixed)
Prime meridian at J2000		W_0	deg	176.63198979682688 (fixed)
Rotation rate		\dot{W}	deg/day	$350.891982490642 \pm 0.000000014$
Quadratic Rotation coefficient		\ddot{W}	deg/day ²	$3.6660\text{e-}12 \pm 9.1\text{e-}13$
Core amplification factor		F	-	0.061 ± 0.006
FCN period		τ_{FCN}	day	-243.0 ± 2.7
LOD variations amplitudes	Viking era	W_{C1}	mas	463 ± 15
		W_{C2}	mas	413 ± 25
		W_{C3}	mas	134 ± 21
		W_{C4}	mas	0 ± 19
		W_{S1}	mas	-318 ± 28
		W_{S2}	mas	483 ± 20
		W_{S3}	mas	53 ± 24
		W_{S4}	mas	39 ± 20
	InSight era	W_{C1}	mas	327.6 ± 1.3
		W_{C2}	mas	320.3 ± 1.3
W_{C3}		mas	115.1 ± 0.8	

		W_{C4}	mas	13.3 ± 0.7
		W_{S1}	mas	-272.2 ± 1.3
		W_{S2}	mas	432.3 ± 2.2
		W_{S3}	mas	52.3 ± 1.4
		W_{S4}	mas	0.2 ± 0.7
Dust parameters		W_{cd}	mas	26 ± 7.3
		W_{sd}	mas	-27 ± 4.9

Supplementary Table S2: Estimated parameters using GINS with the post-dust-storm model (full-arc solution). Uncertainties are 1σ formal errors.

Section 5. Principal moments of inertia

Following Baland et al. (2020)¹¹, the relation between the precession rate of Mars $\dot{\psi}$ and the polar moment of inertia C can be summed up as $C/m_a r_e^2 = -1415393 J_2 / (\dot{\psi} - \dot{\psi}_g)$ where $\dot{\psi}$ and $\dot{\psi}_g$ are expressed in mas/year. $\dot{\psi}_g = 6.754$ mas/year is the geodetic precession. $\dot{\psi}$ is expressed with respect to the Mars mean orbit of epoch J2000. This relation accounts for the external torques exerted by the Sun, Phobos and Deimos, and the other planets, on the oblate shape of Mars. The effects of triaxiality on the precession rate of Mars averages out. Given the precession rate determined in the present study, and the gravity field $J_2 = 0.0019566$ from Konopliv et al. (2020)¹⁰ (MRO120F solution), $C/m_a r_e^2 = 0.36419 \pm 0.00011$, where $m_a = 6.41712 \times 10^{23}$ kg for the mass of Mars¹⁰. The mean moment of inertia is then obtained as $MOI = (C/m_a r_e^2 - 2/3 J_2)(r_e^2/r_a^2) = 0.36428 \pm 0.00011$. $r_e = 3396$ km is the reference radius of the MRO120F solution and $r_a = 3389.5$ km is the mean planetary radius. The principal moments of inertia are $A/m_a r_a^2 = 0.363499$, $B/m_a r_a^2 = 0.363752$, $C/m_a r_a^2 = 0.365589$, with the three of them affected by the same level of uncertainty of 0.00011. Note that there is a typo in Konopliv et al. (2020)¹⁰ for the uncertainty of C , which should be 10 times smaller than the value reported of 0.0006.

Section 6. Equation of state for the liquid core

To model the thermoelastic properties of the liquid core we assume that the liquid Fe-O-S-C-H alloy can be described by an asymmetric Margules mixing model that uses Fe, FeO, FeS, Fe₃C, and FeH as end-members. The volume of the thermodynamic Fe-O-S-C-H solution writes

$$V(p, T) = V_{ideal}(p, T) + V_{ex}(p, T), \quad (S13)$$

where

$$V_{ideal}(p, T) = \sum_{i=\{Fe, FeO, Fe_3C, FeH\}} \chi_i V_i(p, T)$$

and

$$V_{ex}(p, T) = \chi_{Fe} \chi_{FeO} (\chi_{FeO} W_{Fe-FeO} + \chi_{Fe} W_{FeO-Fe}) + \chi_{Fe} \chi_{FeS} (\chi_{FeS} W_{Fe-FeS}(p, T) + \chi_{Fe} W_{FeS-Fe}(p, T)). \quad (S14)$$

The χ_i and $V_i(p, T)$ are the molar fraction and molar volumes of Fe, FeO, FeS, Fe₃C, and FeH, and $\chi_{Fe} = 1 - \chi_{FeO} - \chi_{FeS} - \chi_{Fe_3C} - \chi_{FeH}$. The thermal expansivity and the isothermal bulk modulus of the solution can then be calculated from Eq. (S13) using classical thermodynamic relations. The isobaric heat capacity C_p is computed from the end-members assuming ideality. For the equation of state (EoS) of liquid Fe and liquid FeO we use Dorogokupets et al. (2017)⁶⁶ and Komabayashi (2014)⁶⁷. To describe the elastic properties of FeS and Fe₃C we use the Anderson-Grüneisen EoS^{e.g.67}. The EoS parameters for both end-members have been obtained by fitting the EoS to a large set of experimental data^{68,69,70,71,72,73,74,75,76,109} assuming the thermodynamic model of Xu et al (2021)⁶⁸ for Fe-FeS and ideal mixing for Fe-Fe₃C. The EoS parameters for FeS and Fe₃C are given in

Supplementary Table S3. The Margules coefficients for Fe-FeO can be obtained by deriving Eq.(10) of Komabayashi (2014)⁶⁷ with respect to pressure; those for Fe-FeS are given in Supplementary Table S3. An equation of state for liquid FeH at Mars' core conditions is not available. We therefore use the equation of state describing the volume of interstitial H⁶⁵ in solid iron together with an equation of state of fcc Fe⁶⁶. To take into account the volume difference between the solid and liquid phase, we increase the volume of solid FeH by the relative density difference between liquid and fcc (~2.-2.4%).

	T_0 K	V cm ³ /mol	C_p J/K/mol	α 10 ⁵ /K	K_T GPa	K_T'	γ	δ_T	W_{Fe-X} cm ³ /mol	W_{X-Fe} cm ³ /mol	B_0 GPa	B'
FeS	1650	24.4±0.3	62.5	11.8	12.0±0.8	6.9±0.3	0.62±0.04	0.4±0.5	-9.9±1.4	-3.54±0.4	3.02±0.3	2.6±0.4
Fe ₃ C	1723	26.5±0.1	215.	14.8±5.	57.5±13	15.±3.	1.34±0.4	9.1±4.0	-	-	-	-

Supplementary Table S3: Equation of state parameters for liquid solution end-members and Margules coefficients. For both $\kappa = 1.4$ and X stands for FeS or Fe₃C.

Section 7. Thermal state of the mantle

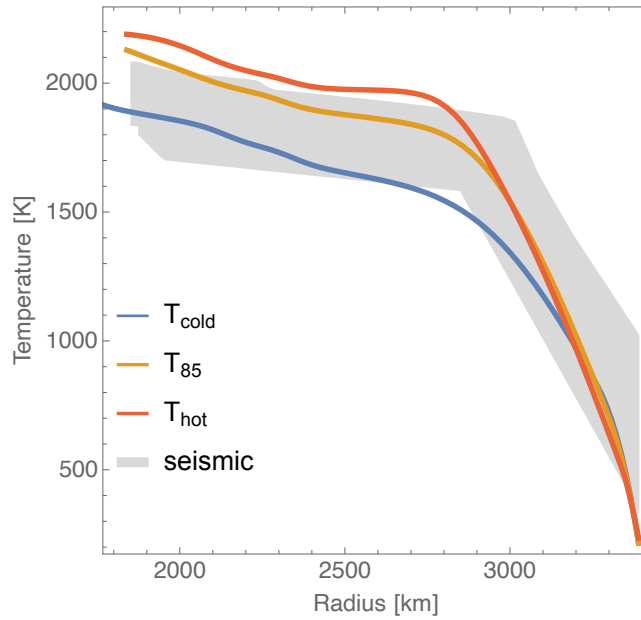
We compute the thermal evolution in a 3D spherical geometry to determine the spatial and temporal evolution of mantle flow throughout Mars' thermal history. In our approach we employ a 3D crust whose thickness variations is derived from gravity and topography data^{20,64}. The temperature distribution in the interior of Mars at present day is the result of 4.5 Gyr of thermal evolution. For our study we use cases 55 and 85 from Plesa et al. (2018)⁷⁷ and an additional case (Moho_2800) that has a crustal structure that agrees with the seismic observations of InSight⁶⁴. The most important parameters of the geodynamical models are listed in

Supplementary Table S4. For a more detailed list of parameters, we refer to the corresponding publications indicated in the footnotes of

Supplementary Table S4. In the following, cases 55, 85, and Moho_2800 will be referred to as T_{cold} , T_{85} , and T_{hot} , respectively. The average present day temperature profiles for the 3 cases are shown in Supplementary Figure S4 together with the temperature range deduced from seismic and geodesy data¹⁷. T_{cold} and T_{hot} are situated close to the lower and upper limit of the seismically deduced temperature range but have a lithosphere thickness that is in the upper range of the latter.

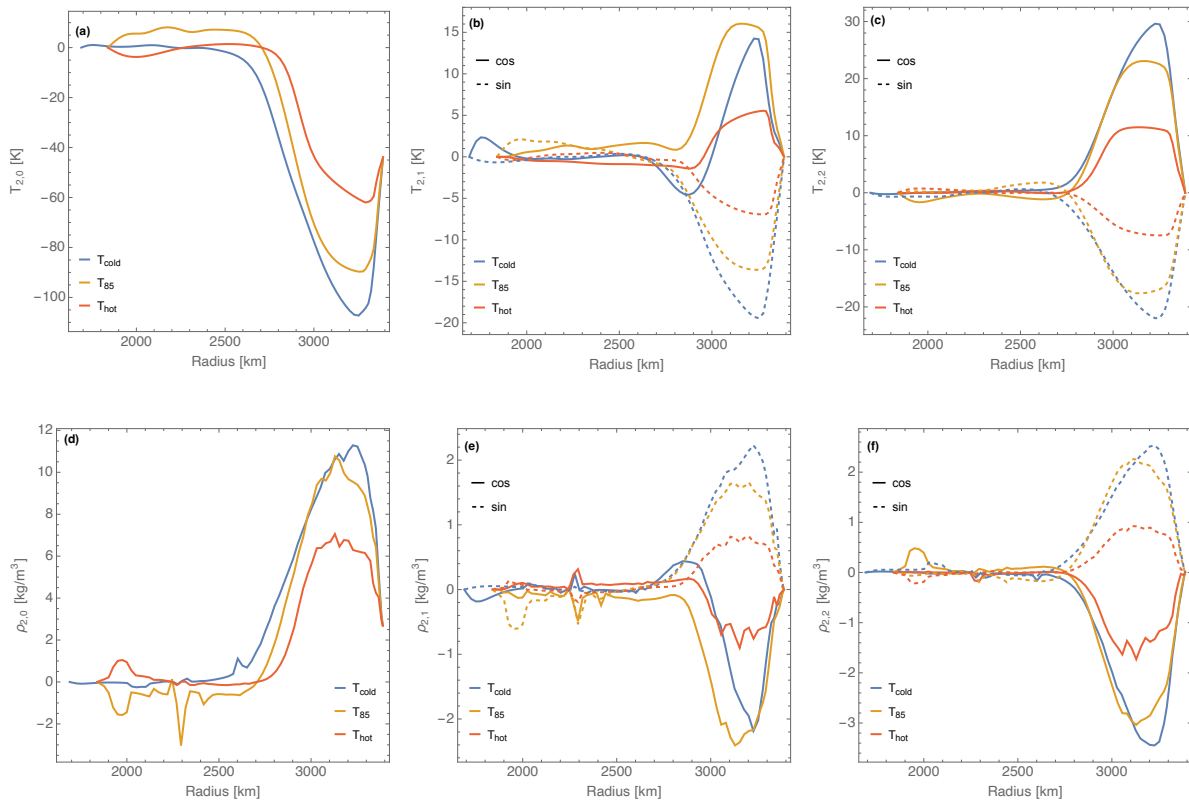
Case	D_{mantle} [km]	η_{ref} [Pa s]	E [kJ/mol]	V [cm ³ /mol]	D_{crust} [km]	ρ_{crust} [kg m ⁻³]	HPE_{crust} [%]
55 ¹ (T_{cold})	1700	1e20	300	6	87.1	3200	93.5
85 ¹ (T_{85})	1550	1e21	325	10	62	3100	67.8
Moho_2800 ² (T_{hot})	1550	1e21.5	300	6	62.2	2800	61.4

Supplementary Table S4: Parameters of the geodynamical thermal evolution models. The mantle thickness is given by D_{mantle} , the reference viscosity is indicated by η_{ref} , D_{crust} describes the average crustal thickness, while ρ_{crust} and HPE_{crust} indicate the crustal density and crustal amount of heat producing elements. 1: Plesa et al. (2018)⁷⁷; 2: Knapmeyer-Endrun et al. (2021)⁶⁴.



Supplementary Figure S4: Temperature profiles from this study (T_{cold} , T_{85} , and T_{hot})^{64,77} and temperature range deduced from geodesy and seismic data¹⁷.

The degree 2 present-day temperature anomalies associated with cases 55, 85, and Moho_2800 are shown in Supplementary Figure S5 (a,b,c). Horizontal temperature fluctuations lead to density anomalies that can affect the shape of the core (Supp: Core shape of non-hydrostatic planet), which directly affects the moments of inertia of the core. The induced degree-2 density anomalies have been calculated from a spherical harmonic expansion of the temperature fields obtained from the 3D thermal evolution calculation for the YMD composition (see Supplementary Figure S5 (d,e,f)) using the software package SHtools⁷⁹.



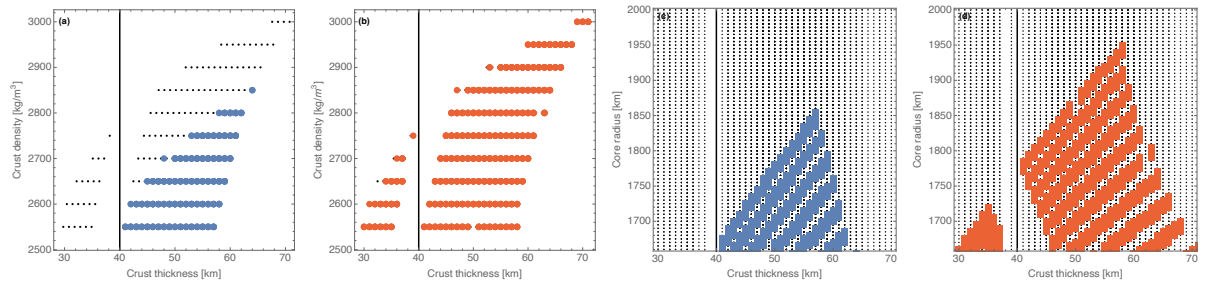
Supplementary Figure S5: Degree 2 and order (0,1,2) cos and sin horizontal temperature anomalies (a,b,c) and induced density anomalies (d,e,f) for the YMD mantle composition for the T_{cold} , T_{85} , and T_{hot} temperatures.

Section 8. Crustal structure

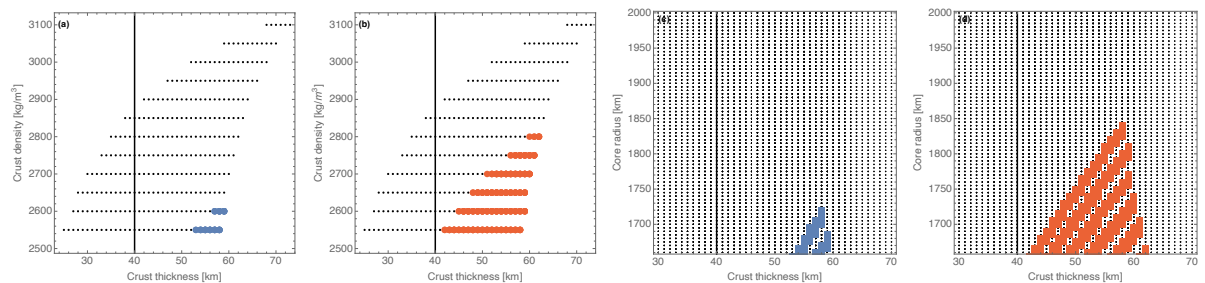
The crustal structure below the InSight lander inferred from seismic data can be used to constrain the thickness and density of the global crust when combined with gravity and topography data⁶⁴. The deduced average crustal density and thickness are correlated and dependent on the density of the uppermost mantle^{20,64}.

The correlation between crustal thickness and density for the YMD and EH45 models have been calculated using the *ctplanet* software⁶³ and the results are shown in Supplementary Figure S6(a,b) and Supplementary Figure S7(a,b) for the 2- and 3- layer crust models compatible with seismic observations. The calculation of the average crustal thickness requires the knowledge of the thickness of the crust below the InSight lander. For both considered cases we use the seismically estimated thickness⁶⁴; 20 ± 5 km for the 2-layer crust and 39 ± 8 km for 3-layer crust.

Only a subset of the interior structure models are found to agree with the moment of inertia of this study (Supplementary Figure S6(c,d) and Supplementary Figure S7(c,d)). Concerning the 2-layer InSight seismic model, only models based on the YMD composition with the hot mantle temperature agree with the moment of inertia. Nevertheless, since those models have a Love number k_2 that does not agree with observations¹⁰, we do not consider them further in this study. Furthermore, we note that recent PP receiver function analyses strongly favor the 3-layer crustal model over the 2-layer model⁸⁰.



Supplementary Figure S6: Crust thickness-density correlation for T_{cold} (a) and T_{hot} (b) mantle temperatures and relation between crust thickness and core radius for mantle temperature T_{cold} (c) and T_{hot} (d) for the mantle composition YMD. The black vertical line delineates the 2 layered (thickness <40km) from the 3 layered (thickness >40km) crust models. Dots correspond to all crustal thickness models that are compatible with the InSight seismic thickness of the crust, whereas colored symbols correspond to the subset of models that are consistent with the moment of inertia.



Supplementary Figure S7: Crust thickness-density correlation for T_{cold} (a) and T_{hot} (b) mantle temperatures and relation between crust thickness and core radius for mantle temperature T_{cold} (c) and T_{hot} (d) for the mantle composition EH45. The black vertical line delineates the 2 layered (thickness <40km) from the 3 layered (thickness >40km) crust models. Dots correspond to all crustal thickness models that are compatible with the InSight seismic thickness of the crust, whereas colored symbols correspond to the subset of models that are consistent with the moment of inertia.

Section 9. Anelasticity, triaxiality, CMB coupling, and Chandler wobble

The compliances β and γ required to compute the core amplification factor F and FCN period (Eq.3 of the main paper) are computed following Dehant and Mathews (2015)³. They are complex valued because the mantle of Mars behaves as an anelastic body at quasi-diurnal periods (nutations periods in the rotating frame). We use a frequency-dependent but depth-independent model of shear dissipation^{e.g.60}. The parameters of the complex shear modulus are chosen such that the semi-diurnal tidal Love number k_2 , the period of the Chandler Wobble, and the secular acceleration of Phobos agree with observations (Tab. S6 of Konopliv et al. (2020)¹⁰). The real parts of $\beta = (0.35 \pm 0.07) 10^{-3}$ and $\gamma = (1.46 \pm 0.15) 10^{-3}$, as shown in Supplementary Figure S8. Mantle anelasticity reduces the FCN

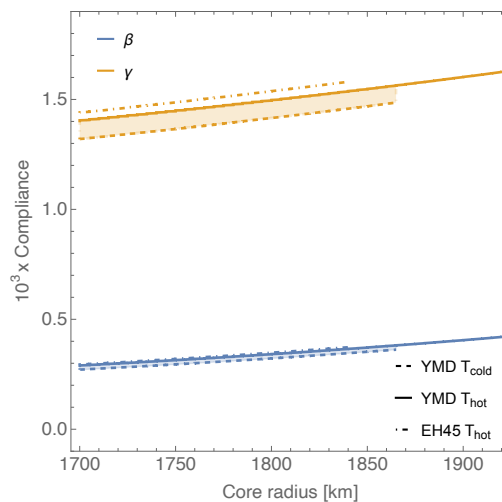
period by about 2%, which is about 2 times larger than the uncertainty, and can be neglected for F , as its effect of less than 1% is small compared to the uncertainty.

The anelastic mantle also leads to a complex valued transfer function (Eq.2 of main paper), which results in the damping of the FCN resonance and to nutations that are out-of-phase with respect to the gravitational forcing. The (-3 degrees) out-of-phase contributions are smaller than 0.02 mas, which is two orders of magnitude smaller than what can be measured by RISE and are therefore neglected in this study.

Besides the anelastic mantle, the viscous coupling of the fluid core to the mantle and the irregular shape of the CMB can affect the period of the FCN of Mars (see Sec. 7.3.3 of Dehant and Mathews (2015)³). The effect of the former, which has been shown to affect the FCN frequency of the Earth by less than 0.1%^{81,82}, is neglected in our study. Topographic coupling is proportional to the square of the small topography at the core-mantle boundary⁸³, it is thus very small and neglected too.

The triaxiality of Mars affects its rotation. Including the effect increases the period of the Chandler Wobble (CW) by about 0.5 days¹⁰ and it has a comparable effect on the FCN period, which decreases by less than 0.5 days (based on Eq.38 of Chen and Shen et al. (2007)⁸⁴). The effect on the FCN is significantly smaller than biaxial non-hydrostatic contributions ($> \sim 7$ days) and can thus be neglected given the 2.7 days uncertainty on the FCN period. The precise effect of triaxiality on the core amplification factor F is currently unknown due to lacking theoretical developments. But it can be roughly estimated by calculating the effect of using the equatorial moments of inertia A or B instead of the average equatorial moment of inertia on F . We find, that F changes by about 2%, which is 5 times smaller than its 1σ uncertainty and is therefore neglected in our study.

Additional to the FCN, the CW rotational normal mode can affect nutation amplitudes (see Dehant and Mathews (2015)³ Eq.7.140 for the full expression of the transfer function). Its period in the inertial frame is about -1.03 days¹⁰, significantly smaller than any of the periods of the main rigid nutations¹¹ and as such is not expected to affect our results in a meaningful way. Using Eq.7.140 for the transfer function instead of Eq.3, shows that the amplitude of the -1/3 annual nutation is reduced by less than 0.5%, an effect that can be neglected given the 10% uncertainty on F .



Supplementary Figure S8: Real part of compliance β and γ for the YMD mantle compositions and the cold (dashed lines) and hot (solid lines) mantle temperature and EH45 for the hot mantle temperature (dot-dashed lines)

Section 10. Core shape of non-hydrostatic planet

Nutation amplitudes depend on the shape of the planet and core mainly through the linear dependence of the FCN frequency on the dynamical flattening of the core (Eqs 2 and 3 of main text). The determination of the core shape of a non-hydrostatic planet requires assumptions about the rheology and about the internal processes generating non-hydrostatic deviations. In a purely static model, the external gravity field and shape of Mars can be explained by assuming that on a long time-scale Mars behaves like a fluid overlain by a solid shell (mechanical lithosphere) with embedded mass anomalies^{20,85}. Compared to the fluid case, the FCN period of a non-hydrostatic planet with a 150 km thick shell is about 4% (10 days) shorter²⁰, which does not agree with RISE observations. Besides static

mass anomalies in the solid shell, the shape of the core can also be affected by dynamic processes in the fluid mantle resulting from mantle convection²².

In the static model^{20,85}, the external shape and gravity field result from the rotational flattening, from the surface topography, and from mass sheet anomalies embedded in the mantle. The first static model is defined by one internal mass sheet located at the crust-mantle interface (Moho). The second static model is defined by one internal mass sheet located just above the bottom of the solid shell. In these two models, the FCN period will agree with the observations if the shell thickness is within a specific range. The third static model is defined by two internal mass sheets located at the Moho and just above the CMB in such a way that the deformation of the core is identical to the one of the hydrostatic model and as such in agreement with the FCN period measured by RISE.

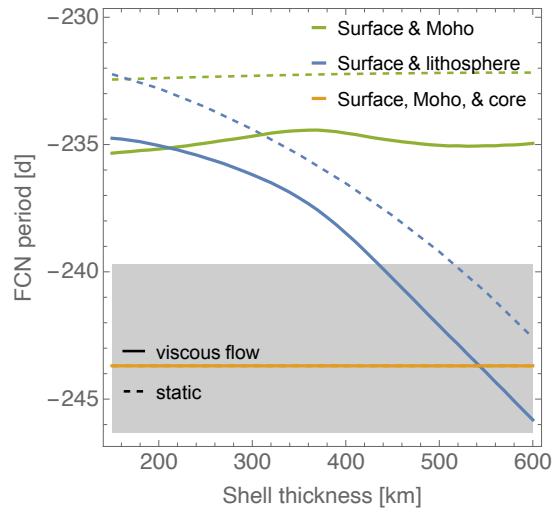
We follow the approach of Zharkov et al. (2009)⁸⁵ to compute the deformation of the CMB due to loads. The procedure consists of four steps. In the first step, solving Clairaut's equation for a given interior model yields the reference hydrostatic shape and gravitational field⁸⁶. Subtracting these from the surface data, we obtain the non-hydrostatic shape and the non-hydrostatic gravitational perturbation at the surface. In the second step, deformations at all depths and gravitational perturbations due to unit-value loads are computed with the well-known load Love number formalism^{e.g.87}. We will first suppose that there are two static loads (surface topography and one internal load either at the Moho or at the bottom of the solid shell), and consider afterwards the case with three static loads. In the third step, the values of the two perturbing loads are determined so that the non-hydrostatic components of the shape and gravity field at harmonic degree 2 agree with data. In the fourth step, the moments of inertia of the core are computed by adding the hydrostatic and non-hydrostatic contributions. The diagonalization of the total inertia tensor yields the principal moments of inertia of the core.

If there are three static loads, the third load (located at the bottom of the mantle) is chosen so that the combined deformation of the three static loads on the core is consistent with the non-hydrostatic components of the core shape deduced from the RISE data. Since the non-hydrostatic components are close to zero (see Supp: Shape and moment of inertia of the core and Supplementary Figure S16), we choose the third load so that the effect of the two other loads is completely compensated.

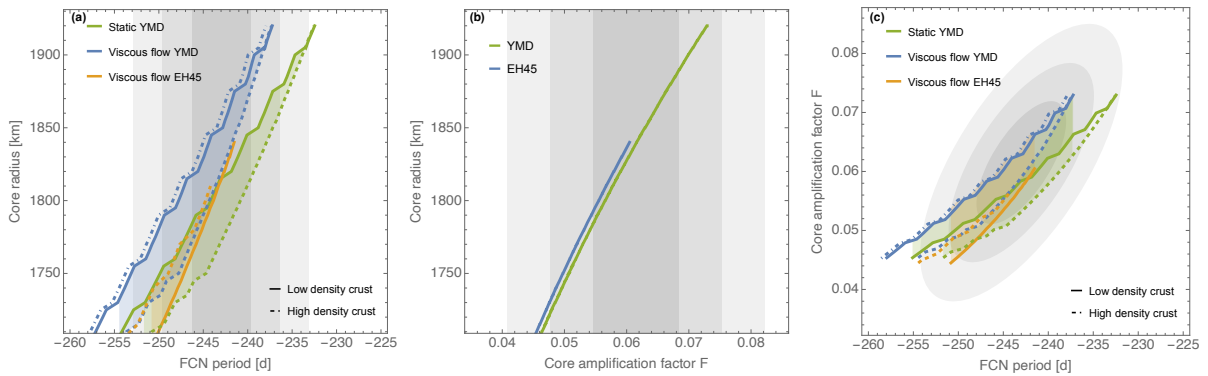
In the dynamic model, the external shape and gravity field result from the perturbations of the static model with two loads, plus a third perturbation due to mantle convection. Mantle convection affects the core shape: its radial deformation is proportional to the discontinuity of the radial stress at the CMB⁸⁸. In practice, viscous flow equations^{89,90} are solved for density perturbations given by a 3D convection model (Supp: Thermal state of the mantle). The surface perturbations (radial and gravitational) due to convection are subtracted from both the observed gravity field and shape of the planet, along with the rotational perturbations in step 1 above. The procedure for calculating the core shape then follows the same course as for the static model. Finally, the deformation of the core-mantle boundary due to convection is added to the deformation due to the static loads before computing the moment of inertia of the core.

We illustrate the effect of the solid shell thickness on the shape of the core for the above loading schemes using an interior model based on the YMD composition and T_{hot} mantle temperature (Supp: Thermal state of the mantle). In this model, the core has a radius of 1815 km and the bottom of the thermal lithosphere is at a depth of 600 km, which corresponds to the largest shell thickness considered in this study. The results show that the thickness of the solid shell has only a small effect on the computed core shape if the load is placed at the depth of the Moho, while the deformation of the core decreases with increasing shell thickness when the load is placed at the bottom of the shell. The viscous flow in the convective mantle reduces the deformation of the core by about 50 m and this effect is only weakly dependent on the shell thickness. When loads are placed at the surface and Moho, the FCN period is predicted to be more than 10 days smaller than the RISE observation irrespective of the shell thickness (Supplementary Figure S9). When the second load is placed at the bottom of the solid shell, the FCN period matches the RISE observation only if it is thicker than about 512 km in the static setting, and about 426 km when dynamic convective effects are considered (viscous flow setting). The thinnest of these two values is comparable to the present-day elastic thickness beneath the north polar cap, which is predicted to lie between 330 and 450 km⁹¹.

A comparison between the static and viscous flow setting for the interior structure models used in this study is shown in Supplementary Figure S10. Including the effect of viscous flow decreases the FCN period by about 5 days, which is comparable to the effect of changing the crust density from its highest to its lowest allowed value.



Supplementary Figure S9: FCN period as a function of shell thickness for loads placed at the surface and Moho, surface and bottom of the shell, and surface, Moho, and core for static (dashed curve) and viscous flow (solid curve) deformation. The gray shaded region represents the 1σ limits of the FCN period observed by RISE.



Supplementary Figure S10: (a) Core radius as a function of FCN period, (b) core radius as a function of core amplification factor, and (c) FCN period-core amplification correlation for the YMD and EH45 (only viscous flow) mantle composition and T_{hot} mantle temperature for loads placed at the surface and bottom of the lithosphere for the static and viscous flow setting. Solid and dashed curves represent models with an adiabatic core temperature and the dot-dashed curves assume an isothermal core temperature (thick crust+viscous flow). The gray shaded areas represent 1σ , 2σ , and 3σ uncertainties.

Section 11. Enriched basal silicate layer (BSL)

Like many terrestrial planets that differentiated into a metallic core and a silicate mantle, Mars probably experienced an early global magma ocean stage. The crystallization and the differentiation of a magma ocean can lead to the formation of a compositionally distinct layer at the bottom of the mantle⁹², strongly enriched in heat-producing elements (HPE) and iron, leading to its long-term stability with little mixing between the layer and the overlying mantle^{93,94,95}. The presence of an enriched basal silicate layer (BSL) can strongly affect the evolution of the planet and its current state. In particular, the basal layer can give rise to the presence of a molten silicate layer above the core that can act as a deep seismic reflector and be interpreted as an extension of the liquid core²³. The relative rotation of this effective liquid core (metallic core + molten silicate layer) with respect to the mantle affects the nutation of Mars and as such is responsible for the signature of the core measured by RISE.

Following Samuel et al. (2019)⁹⁶ we compute the thermo-chemical evolution of a set of models that incorporate a BSL. The mantle is composed of a basal layer of thickness D_d enriched in iron and in heat producing elements that is overlain by a more depleted convecting mantle. The BSL is at least 10% denser than the overlying mantle and its density increases with depth, making it stable against convection. The insulating effect and the HPE enrichment of the BSL can lead to a partially or fully molten region in its lowermost part. If the melt fraction is above the critical value of 40%^{101,102} the rheological behavior of that region is effectively that of a liquid, i.e. with a zero shear modulus. For smaller melt fractions, the partially molten region behaves as a soft, yet essentially solid (i.e., mushy) material of thickness D_{mush} with reduced but non-zero shear modulus. BSL models with a fully molten

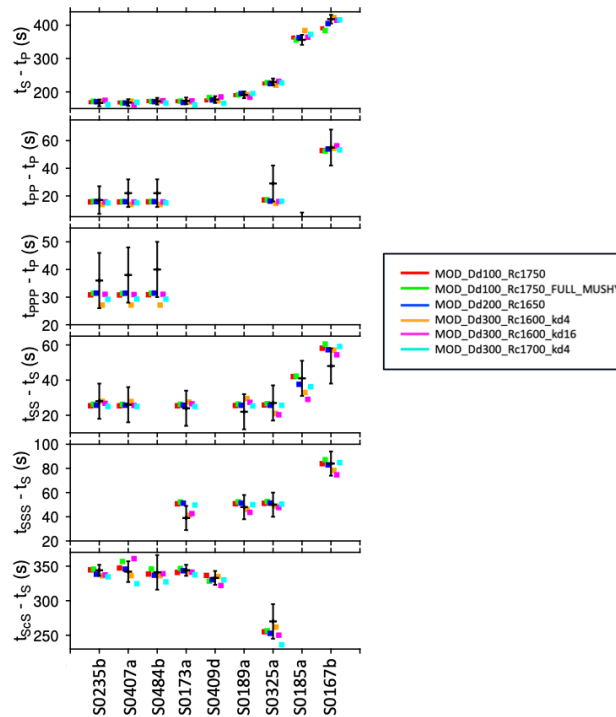
lower part of thickness D_{liquid} have an apparent liquid core radius of $R_{liquid} = R_c + D_{liquid}$ that is compatible with the core radius range inferred from seismic data¹⁷. Following Drilleau et al. (2021)¹⁰³, we ascertained that our BSL models are also consistent with the differential arrival times (Supplementary Figure S11) of body waves (tS-tP, tPP-tP, tPPP-tP, tSSS-tS, tSS-tS, tScS-tS) observed by the seismometer on InSight^{17,78} and their inferred locations¹⁷ as well as the velocity structure in the 3 layered crust⁶⁴. All models match the moment of inertia of Mars¹⁰, have an average crustal thicknesses that is within the bounds inferred from receiver functions and gravity data⁶⁴, and are compatible with the recent volcanism observed for Mars^{97,98}.

BSL models require a liquid lower mantle layer to agree with the RISE observations. They have a thermal lithosphere between 260 km and about 315 km which are significantly thinner than those of the other models considered in this study. Therefore, the effect of a load placed at the bottom of the lithosphere on the FCN period is comparable to one placed at the Moho depth. Even with a load placed at a shallower depth, BSL models agree with the RISE data, mainly because the large core deformation induced by the Moho load (Supp: Core shape of non-hydrostatic planet) is strongly reduced by the compliance β (see Eq.3) because of the mushy lower mantle. Note that for all models considered, a lithosphere of the thickness of the thermal lithosphere has been assumed. The key governing parameters of our models are listed in Supplementary Table S5.

The apparent core radius of models with a fluid layer at the bottom of the mantle that are compatible with RISE agrees with the range deduced from models without a fluid basal layer from this study. RISE data cannot differentiate between models that have a thin or thick fluid basal layer.

Model	R_c [km]	D_d [km]	T_{m0} [K]	T_{c0} [K]	k_d [W/m/K]	V^* [cm ³ /mol]	η_0 [Pa s]	D_{liquid} [km]	D_{mush} [km]	D_{solid} [km]
Rc1750_Dd100	1750	100	1800	2100	8	7	10^{21}	39	61	0
Rc1750_Dd100_kd6	1750	100	1700	2000	6	7	$3 \cdot 10^{20}$	0	73	27
Rc1400_Dd200	1400	200	1800	2100	8	7	10^{21}	171	29	0
Rc1650_Dd200	1650	200	1800	2100	8	7	10^{21}	122	28	50
Rc1600_Dd300_kd4	1600	300	1800	2000	4	4	10^{21}	273	27	0
Rc1600_Dd300_kd16	1600	300	1800	2000	16	4	10^{21}	247	53	0
Rc1700_Dd300_kd4	1700	300	1800	2000	4	4	10^{21}	173	27	100

Supplementary Table S5: BSL models key parameters: Core radius (R_c), BSL thickness (D_d), initial uppermost mantle (T_{m0}) and core temperatures (T_{c0}), BSL thermal conductivity (k_d), effective activation volume (V^*) and reference viscosity (η_0) of the mantle, thicknesses of molten layer (D_{liquid}), mushy layer (D_{mush}), and solid layer (D_{solid}) within the BSL.



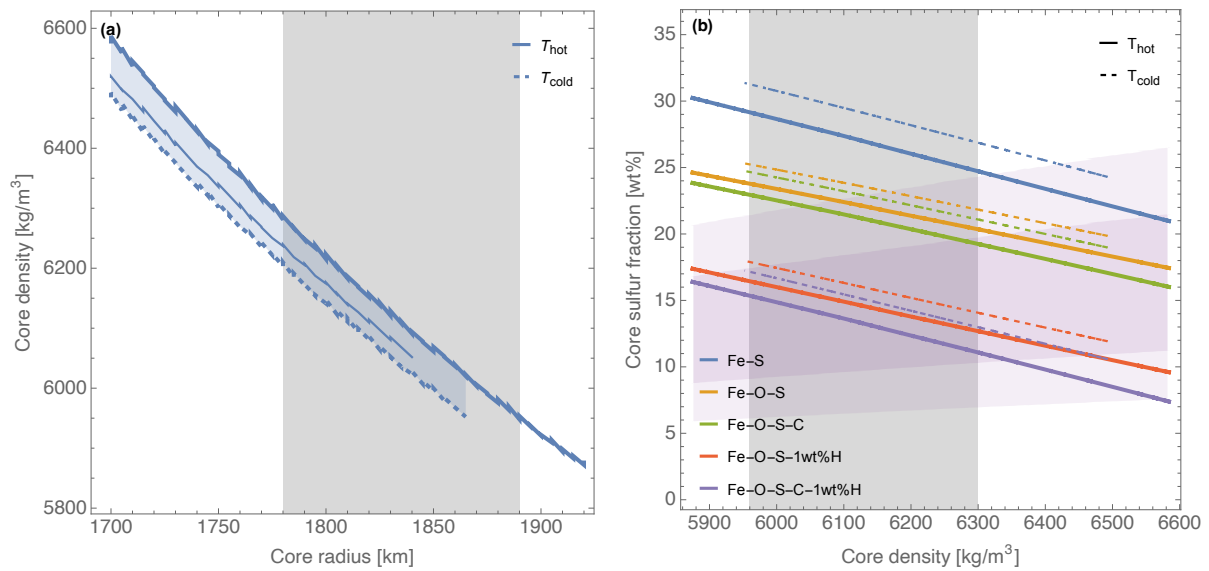
Supplementary Figure S11: Arrival times of the BSL models for the nine considered quakes (colored dots). The measured arrival times (black symbols) are shown with 1σ error-bars.

Section 12. Core structure and composition

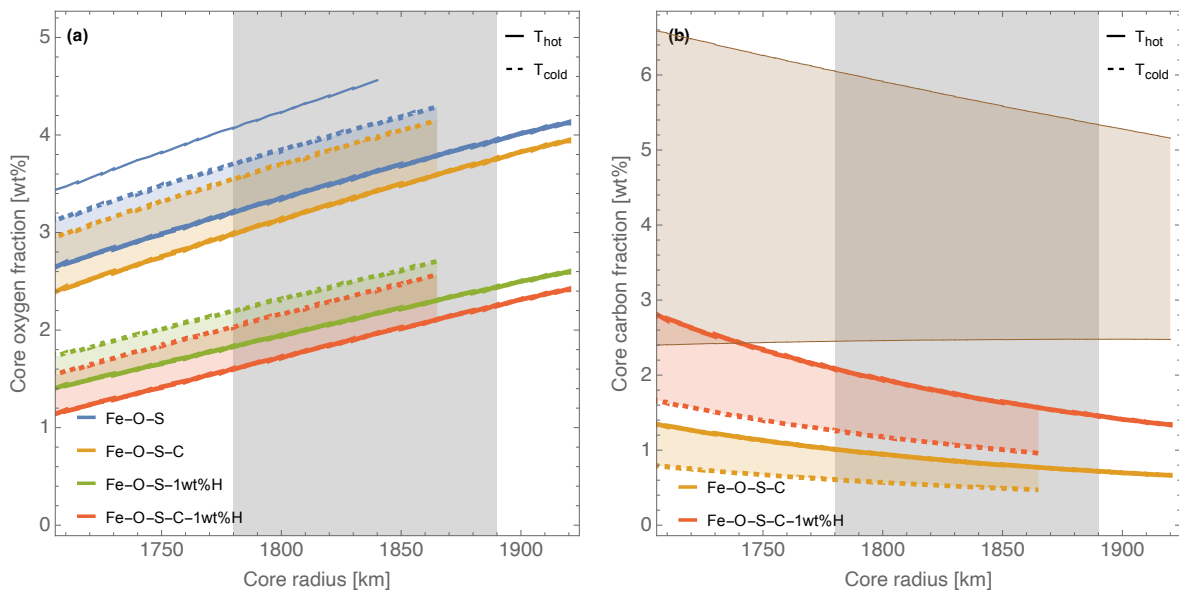
The average density of the core of the models with the YMD or EH45 mantle compositions that agree with RISE are between about 5955-6290 kg/m³ (Supplementary Figure S12a). This range is narrower than the 5700-6300 kg/m³ range advocated by¹⁷, and our lower bound is significantly higher. The main reason for this difference results from the uppermost mantle density that can be appreciably higher in models deduced from seismic data that are based on the so-called geophysical approach¹⁷. In this approach, a layer with constant density in the uppermost part of the mantle is modeled directly from the inferred seismic velocities⁷⁸ while density should vary with depth as the case if it were related to composition and temperature. Other less important factors that affect the density of the core result from the wider spread of mantle temperatures (Supp: Thermal state of the mantle) and the larger set of mantle compositions considered in Stähler et al. (2021)¹⁷ (Lodders and Fegley (1997)¹⁰⁴, EH45¹³, Taylor (2013)¹⁰⁵, YMD¹⁴). We don't use the models of Lodders and Fegley (1997)¹⁰⁴ and Taylor (2013)¹⁰⁵ since the latter does not agree with the crust structure and the moment of inertia of Mars and the former leads to results that are equivalent to those based on EH45⁶⁴. Note that, given the mass conservation, the differences in mantle density directly reflect on the density jump at the core mantle boundary (Supplementary Figure S14). Models that agree with RISE data have a density jump of 1694-2108 kg/m³. Because of the larger average core density found in this study, the required fraction of light elements in the core is appreciably lower than in Stähler et al. (2021)¹⁷ (see their Fig. 2 and Fig. S11-1b) and in particular, up to 5 wt% O and 2 wt% H are not required if the amount of S is limited to the range deduced from cosmochemical considerations²⁵. The fraction of O in the core increases with S, which increases with core radius (Supplementary Figure S13a), and is larger for EH45 models than YMD models since the former have a larger fraction of FeO in the mantle²⁶. The amount of C that can dissolve in the core at core-mantle boundary conditions increases with decreasing amount of S (Supplementary Figure S13b) and is about two times larger if the core contains 1wt% of H. As a result of the required large fraction of S, the maximal amount of C that can dissolve in the core is below predictions based on an assumed bulk C content (e.g. 1-1.4wt%²⁵) and its partitioning behavior between molten metal and silicate ($\log(D_c^{met-sil}) \sim 0.5 - 2.5$ ^{58,106}) at core-mantle boundary conditions (Supplementary Figure S13b). The precise temperature profile in the core is not known and is likely between an isotherm and adiabat^{e.g.53}. Using an isothermal temperature profile in the core increases the fraction of light elements by up to about 0.5 wt% if compared to a calculation with an adiabatic temperature profile. The effect of this difference in light elements decreases the density jump at the CMB by less than 3% and decreases the moment of inertia of the core by less than 0.2%. Those combined effects decrease the FCN period by up to 0.6 day (Supplementary Figure S10) and increase *F* by up to 0.3%. Since those effects are small compared to the uncertainties at 1 σ , for convenience we assume an adiabatic temperature profile in the core for the calculation of the FCN period and *F* and for the discussion related to the composition of the core.

The large fraction of light elements in the core (Figure 4 of main paper, Supplementary Figure S13) makes the presence of an inner core highly unlikely. The melting temperature of Fe-O-S-C-H alloys at Mars core conditions is not well known, but an upper bound can be roughly estimated by cumulating the effect that each individual light element has on the melting temperature of Fe. As long as the composition of the alloy is on the iron-rich side of the eutectic, the addition of light elements to Fe results in a decrease of its melting temperature. If the core has a radius of 1835 km, as found in this study, about 2.5 wt%O, 15 wt%S, 1.5 wt%C, and 1 wt%H are required to match its density. At core center pressures (~40 GPa), adding 15 wt% of S decreases the melting temperature of Fe (2800 K¹⁰⁷) by ~1000 K¹⁰⁸, whereas individually 2.5 wt%O, 1.5 wt%C, and 1 wt%H result in temperature reductions of ~250 K⁶⁷, ~255 K¹⁰⁹ and ~220 K¹¹⁰, respectively. The cumulative effect of all those light elements results in a melting temperature at the center of the core that is significantly below the core temperature (1880 K - 2400 K).

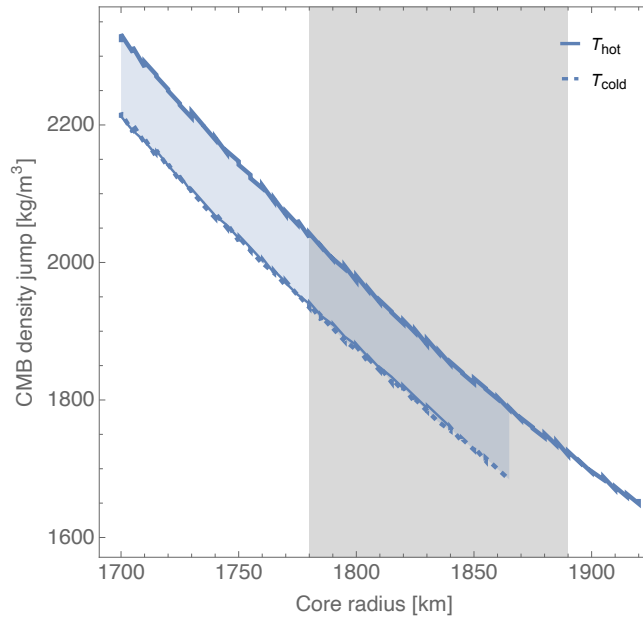
The amount of light elements in the core can be lower if the mantle is less dense than assumed above, for example by having a lower FeO content or a higher temperature. Temperatures significantly above our hot end-member model are, however, unlikely (Supp: Thermal state of the mantle) and the effect of decreasing the weight fraction of FeO in the mantle has only a small effect of the order of 1 wt% on the amount of light elements (main text Fig. 4), as follows from a comparison of the EH45 and YMD models (17.7 wt% vs. 14.7 wt% FeO in the mantle). We nevertheless note that the effect of the lower amount of FeO in the mantle is reduced by the more massive crust of the YMD models compared with EH45 models (Supp: Crustal structure) and the tradeoff between mantle FeO and O-S content in the core²⁶.



Supplementary Figure S12: (a) Average core density as a function of core radius for the YMD mantle composition with the T_{hot} and T_{cold} mantle temperatures (thick lines) and for the EH45 mantle composition with the T_{hot} temperature profile (thin line). The gray area represents the core radius of this study (1σ). (b) Relation between core density and core composition for the YMD mantle composition and the T_{hot} and T_{cold} temperature profiles. The gray array represents the core density range that agrees with the core radius of this study. The light purple area is the core S content following cosmochemical considerations²⁵ and the lighter purple area assumes that the S content of Mars is equivalent to chondrites (1.6-5.6 wt%)³².



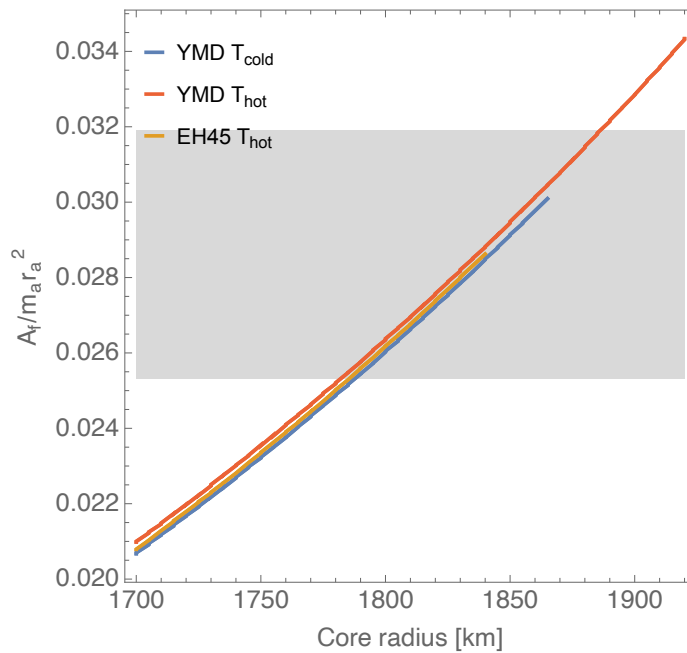
Supplementary Figure S13: Core oxygen (a) and carbon fraction at its solubility limit at core-mantle boundary conditions (b) for T_{hot} and T_{cold} . The gray area represents the core radius of this study (1σ). YMD models are represented by the thick curve and the thin curve represents the EH45 models with the T_{hot} profile. The brownish area in (b) represents the C content in the core assuming a bulk content range and the partition behavior of C between the liquid core and molten mantle at core-mantle boundary conditions (see text).



Supplementary Figure S14: Density jump at the CMB for the T_{hot} and T_{cold} . The gray area represents the core radius of this study (1σ). YMD models are represented by the thick curves and the thin curve represents the EH45 models with the T_{hot} profile.

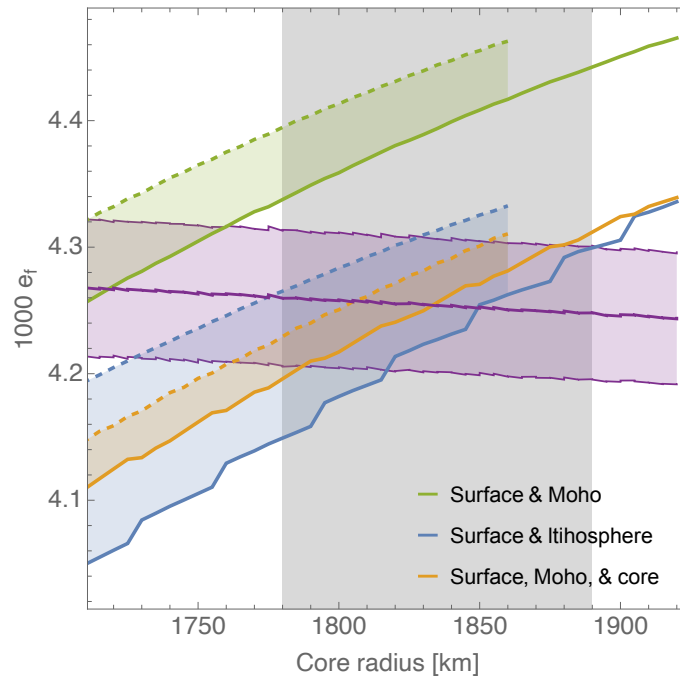
Section 13. Shape and moment of inertia of the core

The moment of inertia of the core can be obtained from F (Eq.3 in the main paper) but it requires to know the compliance γ . Forward modeling shows that the models of this study and models with a dense fluid lower mantle layer (Supp: Core structure and composition) have a γ between $1.4 \cdot 10^{-3}$ and $1.62 \cdot 10^{-3}$ if they agree with the k_2 Love number at 1σ . We can take into account our lack of knowledge about γ if we assume that it is a random variate with an uniform distribution between $1.4 \cdot 10^{-3}$ and $1.62 \cdot 10^{-3}$. The moment of inertia of the core can then be estimated by Monte Carlo error propagation if we assume that F and the principal moments of inertia of Mars have a normal distribution around their mean value. We find that $A_f/m_a r_a^2 = 0.0286 \pm 0.0033$ (11%). The moment of inertia of the core of our interior models is shown in (Supplementary Figure S15).



Supplementary Figure S15: Normalized core moment of inertia for the YMD composition with the hot and cold temperature and EH45 composition with the hot mantle temperature. The gray shaded area represents the value of A_f estimated from F (1σ).

The dynamical core flattening e_f of the Mars models used in this study can be estimated from the measured FCN period and compliance β using (Eq.3 of the main paper). Models that agree with the core flattening (Supp: Core shape of non-hydrostatic planet) require either a thick lithosphere with a mass anomaly placed at the bottom or at the Moho and bottom of the mantle (see Supplementary Figure S16) both together with the load induced by the crust at the surface. Note that for the latter case the load at the bottom of the mantle is set such that the combined deformation of the surface and Moho load on the core is cancelled, i.e. the core has the shape of a hydrostatic planet.



Supplementary Figure S16: Dynamic core flattening in agreement with RISE data as a function of core radius (purple area) compared to models with the YMD mantle composition that have loads at the surface & Moho, surface & lithosphere, and surface, Moho & core. Dashed curves represent models with the hot temperature profile and dashed curves are for cold temperature. The gray shaded area represents the core radius deduced from the core amplification factor F of this study (1σ). Models with loads placed at the surface, Moho & core have the core flattening of a hydrostatic planet.

Supplementary references

1. W. B. Banerdt, S. E. Smrekar, D. Banfield, D. Giardini, M. Golombek, C. L. Johnson, P. Lognonné, A. Spiga, T. Spohn, C. Perrin, S. C. Stähler, D. Antonangeli, S. Asmar, C. Beghein, N. Bowles, E. Bozdog, P. Chi, U. Christensen, J. Clinton, G. S. Collins, I. Daubar, V. Dehant, M. Drilleau, M. Fillingim, W. Folkner, R. F. Garcia, J. Garvin, J. Grant, M. Grott, J. Grygorczuk, T. Hudson, J. C. E. Irving, G. Kargl, T. Kawamura, S. Kedar, S. King, B. Knapmeyer-Endrun, M. Knapmeyer, M. Lemmon, R. Lorenz, J. N. Maki, L. Margerin, S. M. McLennan, C. Michaut, D. Mimoun, A. Mittelholz, A. Mocquet, P. Morgan, N. T. Mueller, N. Murdoch, S. Nagihara, C. Newman, F. Nimmo, M. Panning, W. T. Pike, A.-C. Plesa, S. Rodriguez, J. A. Rodriguez-Manfredi, C. T. Russell, N. Schmerr, M. Siegler, S. Stanley, E. Stutzmann, N. Teanby, J. Tromp, M. van Driel, N. Warner, R. Weber, M. Wiczeorek, Initial results from the InSight mission on Mars. *Nat. Geosci.* **13**, 183–189 (2020).
2. W.M. Folkner, V. Dehant, S. Le Maistre, M. Yseboodt, A. Rivoldini, T. Van Hoolst, S.W. Asmar, M.P. Golombek, The rotation and interior structure experiment on the InSight mission to Mars. *Space Sci. Rev.* **214** (5), 100 (2018).
3. V. Dehant, V., P.M. Mathews, Ed., Precession, Nutation and Wobble of the Earth, *Cambridge University Press*, Cambridge (2015).
4. T. Sasao, S. Okubo, M. Saito, A simple theory on dynamical effects of stratified fluid core upon nutational motion of the Earth, *Proc. IAU Symposium* **78**, 165–183 (1980).
5. W.M. Folkner, C.F. Yoder, D.N. Yuan, E.M. Standish, R.A. Preston, Interior structure and seasonal mass redistribution of Mars from radio tracking of Mars pathfinder. *Science* **278** (5344), 1749–1752 (1997).
6. C.F. Yoder, E.M. Standish, Martian precession and rotation from Viking lander range data. *J. Geophys. Res.* **102**(E2), 4065–4080 (1997).
7. S. Evans, W. Taber, T. Drain, J. Smith, H.-C. Wu, M. Guevara, R. Sunseri, J. Evans, MONTE: The next generation of mission design and navigation software. *CEAS Space J.* **10**, 79–86 (2018).
8. J.C. Marty, S. Loyer, F. Perosanz, F. Mercier, G. Bracher, B. Legresy, L. Portier, H. Capdeville, F. Fund, J.M. Lemoine, GINS: The CNES/GRGS GNSS scientific software, *In 3rd Int. Coll. Sci. Fundam. Asp. Galileo Program. ESA proceedings WPP326* **31**, 8-10 (2011).
9. S. Le Maistre, P. Rosenblatt, A. Rivoldini, V. Dehant, J.-C. Marty, O. Karatekin, Lander radio science experiment with a direct link between Mars and the Earth. *Planet. Space Sci.* **68**, 105–122 (2012).
10. A. S. Konopliv, R. S. Park, A. Rivoldini, R.-M. Baland, S. Le Maistre, T. Van Hoolst, M. Yseboodt, V. Dehant, Detection of the Chandler Wobble of Mars From Orbiting Spacecraft. *Geophys. Res. Lett.* **47**, e2020GL090568 (2020).
11. R.-M. Baland, M. Yseboodt, S. Le Maistre, A. Rivoldini, T. Van Hoolst, V. Dehant, The precession and nutations of a rigid Mars. *Celest Mech Dyn Astr* **132**, 47 (2020).
12. D. Banfield, J.A. Rodriguez-Manfredi, C.T. Russell, K.M. Rowe, D. Leneman, H.R. Lai, P.R. Cruce, J.D. Means, C.L. Johnson, S.P. Joy, P.J. Chi, I.G. Mikellides, S. Carpenter, S. Navarro, E. Sebastian, J. Gomez-Elvira, J. Torres, L. Mora, V. Peinado, A. Lepinette, K. Hurst, P. Lognonné, S.E. Smrekar, W.B. Banerdt, InSight Auxiliary Payload Sensor Suite (APSS). *Space Sci. Rev.* **215**(1), 1-33 (2019).
13. C. Sanloup, F. Guyot, P. Gillet, G. Fiquet, M. Mezouar, I. Martinez, Density measurements of liquid Fe-S alloys at high pressure. *Geophys. Res. Lett.* **27**, 811 (1999).
14. T. Yoshizaki, W. F. McDonough, The composition of Mars, *Geochim. Cosmochim. Acta* **273**, 137–162 (2020).
15. S.E. Smrekar, P. Lognonné, T. Spohn, W.B. Banerdt, D. Breuer, U. Christensen, V. Dehant, M. Drilleau, W. Folkner, N. Fuji, R.F. Garcia, D. Giardini, M. Golombek, M. Grott, T. Gudkova, C. Johnson, A. Khan, B. Langlais, A. Mittelholz, A. Mocquet, R. Myhill, M. Panning, C. Perrin, W.T. Pike, A.C. Plesa, A. Rivoldini, H. Samuel, S. Staehler, T. Van Hoolst, M. van Driel, O. Verhoeven, R. Weber, M. Wiczeorek, Pre-mission InSights on the Interior of Mars. *Space Sci Rev.* **215**, 3 (2019).
16. C. F. Yoder, A. S. Konopliv, D. N. Yuan, E. M. Standish, W. M. Folkner, Fluid core size of Mars from detection of the solar tide. *Science* **300**, 299–303 (2003).

17. S. C. Stähler, A. Khan, W. B. Banerdt, P. Lognonné, D. Giardini, S. Ceylan, M. Drilleau, A. C. Duran, R. F. Garcia, Q. Huang, D. Kim, V. Lekic, H. Samuel, M. Schimmel, N. Schmerr, D. Sollberger, É. Stutzmann, Z. Xu, D. Antonangeli, C. Charalambous, P. Davis, J. C. E. Irving, T. Kawamura, M. Knapmeyer, R. Maguire, A. G. Marusiak, M. P. Panning, C. Perrin, A.-C. Plesa, A. Rivoldini, C. Schmelzbach, G. Zenhäusern, É. Beucler, J. Clinton, N. Dahmen, M. van Driel, T. Gudkova, A. Horleston, W. T. Pike, M. Plasman, S. E. Smrekar, Seismic detection of the martian core. *Science* **373**, 443–448 (2021).
18. A. Rivoldini, T. Van Hoolst, O. Verhoeven, A. Mocquet, V. Dehant, Geodesy constraints on the interior structure and composition of Mars. *Icarus* **213**, 451–472 (2011).
19. A. Khan, C. Liebske, A. Rozel, A. Rivoldini, F. Nimmo, J. A. D. Connolly, A.-C. Plesa, D. Giardini, A geophysical perspective on the bulk composition of Mars. *J. Geophys. Res.* **123**, 575–611 (2018).
20. M. A. Wieczorek, M. Beuthe, A. Rivoldini, T. Van Hoolst, Hydrostatic interfaces in bodies with nonhydrostatic lithospheres. *J. Geophys. Res. Planets* **124**, 1410–1432 (2019).
21. W.S. Kiefer, B.G. Bills, R.S. Nerem, An inversion of gravity and topography for mantle and crustal structure on Mars. *J. Geophys. Res. Planets* **101**, 9239 (1996).
22. P. Defraigne, V. Dehant, T. Van Hoolst, Steady-state convection in Mars' mantle. *Planet. Space Sci.*, **49**, 501–509 (2001).
23. H. Samuel, M. D. Ballmer, S. Padovan, N. Tosi, A. Rivoldini, A.-C. Plesa, The Thermo-Chemical Evolution of Mars With a Strongly Stratified Mantle. *J. Geophys. Res. Planets* **126**, e2020JE006613 (2021).
24. A. K. McNamara, A review of large low shear velocity provinces and ultra low velocity zones. *Tectonophysics* **760**, 199–220 (2019).
25. E. S. Steenstra, W. van Westrenen, A synthesis of geochemical constraints on the inventory of light elements in the core of Mars. *Icarus* **315**, 69–78 (2018).
26. H. Gendre, J. Badro, N. Wehr, S. Borensztajn, Martian core composition from experimental high-pressure metal-silicate phase equilibria. *Geochemical Perspectives Letters*, **21**, 42-46 (2022).
27. Y. Shibazaki, E. Ohtani, H. Terasaki, A. Suzuki, K. Funakoshi, Hydrogen partitioning between iron and ringwoodite: Implications for water transport into the Martian core. *Earth Planet. Sci. Lett.* **287**, 463–470 (2009).
28. V.N. Zharkov, The Internal Structure of Mars: A Key to Understanding the Origin of Terrestrial Planets, *Sol. Syst. Res.* **30**, 456-46 (1996).
29. K. Tsuno, D.J Frost, D.C. Rubie, The effects of nickel and sulphur on the core-mantle partitioning of oxygen in Earth and Mars. *Phys. Earth Planet. Inter.* **185**, 1–12 (2011).
30. P. Defraigne, A. Rivoldini, T. Van Hoolst, V. Dehant, Mars nutation resonance due to free inner core nutation. *J. Geophys. Res., Planets* **108**(E12), 5128 (2003).
31. A. Mittelholz, C. L. Johnson, J. M. Feinberg, B. Langlais, R. J. Phillips, Timing of the martian dynamo: New constraints for a core field 4.5 and 3.7 Ga ago. *Sci. Adv.* **6**, 18 (2020).
32. K. Lodders, Relative atomic solar system abundances, mass fractions, and atomic masses of the elements and their isotopes, composition of the solar photosphere, and compositions of the major chondritic meteorite groups. *Space Sci Rev*, **217**(3), 44 (2021).
33. D. Kahan, W. M. Folkner, D. R. Buccino, V. Dehant, S. Le Maistre, A. Rivoldini, T. Van Hoolst, M. Yseboodt, J. C. Marty, Mars precession rate determined from radiometric tracking of the InSight lander. *Planet. Space Sci.* **199**, 105208 (2021).
34. M. Yseboodt, V. Dehant, M.J. Péters, Signatures of the Martian rotation parameters in the Doppler and range observables. *Planet. Space Sci.* **144**, 74–88 (2017).
35. J.A. Estefan and O.J. Sovers, JPL Publication **94-24** (1994)

36. S. Le Maistre, Martian Lander Radio Science Data Calibration for Mars Troposphere. *Radio Science*, **55**(12), 1–16 (2020).
37. D. Buccino, J.S. Border, W.M. Folkner, D. Kahan, S. Le Maistre, Low-SNR Doppler Data Processing for the InSight Radio Science Experiment. *Remote Sensing*. **14**(8), 1924 (2022).
38. S. Le Maistre, P. Rosenblatt, V. Dehant, J.-C. Marty, M. Yseboodt, Mars rotation determination from a moving rover using Doppler tracking data: What could be done? *Planet. Space Sci.* **159**, 17-27 (2018).
39. W. M. Folkner, J. G. Williams, D. H. Boggs, R. S. Park, P. Kuchynka, The planetary and lunar ephemerides DE430 and DE431, *Interplanetary Network Progress Rep.* **42**, 196 (2014).
40. R. A. Jacobson, V. Lainey, Martian satellite orbits and ephemerides. *Planetary and Space Science*. **102**, 35-44 (2014).
41. V. Dehant, P. Defraigne, and T. Van Hoolst, Computation of Mars' transfer functions for nutations, tides and surface loading. *Physics of the Earth and Planetary Interiors*, **117**, 385–395, January 2000.
42. T. Van Hoolst, V. Dehant, F. Roosbeek, and P. Lognonné, Tidally induced surface displacements, external potential variations, and gravity variations on Mars. *Icarus*, **161**, 281–296, 2 2003.
43. B. A. Archinal, C. H. Acton, M. F. A'Hearn, A. Conrad, G. J. Consolmagno, T. Duxbury, D. Hestroffer, J. L. Hilton, R. L. Kirk, S. A. Klioner, D. McCarthy, K. Meech, J. Oberst, J. Ping, P. K. Seidelmann, D. J. Tholen, P. C. Thomas, I. P. Williams, Report of the IAU Working Group on Cartographic Coordinates and Rotational Elements: 2015. *Celestial Mech. Dyn. Astron.* **130**, 22 (2018).
44. A.S. Konopliv, C.F. Yoder, E.M. Standish, D.-N. Yuan, W.L. Sjogren, A global solution for the Mars static and seasonal gravity, Mars orientation, Phobos and Deimos masses, and Mars ephemeris. *Icarus* **182**(1), 23–50 (2006).
45. V. Dehant, S. Le Maistre, R.-M. Baland, Ö. Karatekin, M.-J. Péters, A. Rivoldini, T. van Hoolst, M. Yseboodt, M. Mitrovic, the LaRa team, The radioscience LaRa instrument onboard ExoMars 2020 to investigate the rotation and interior of Mars. *Planetary and Space Science*, **180**, 104776 (2020).
46. R.-M. Baland, A. Hees, M. Yseboodt, A. Bourgoïn, S. Le Maistre, Relativistic contributions to the rotation of Mars. *in press, Astronomy and Astrophysics* (2022).
47. L. Lange, F. Forget, D. Banfield, M. Wolff, A. Spiga, E. Millour, D. Viúdez-Moreiras, A. Bierjon, S. Piqueux, C. Newman, J. Pla-García, W.B. Banerdt, Insight pressure data recalibration, and its application to the study of long-term pressure changes on mars. *J. Geophys. Res., Planets* **127** (2022).
48. J.M. de la Torre, S. Piqueux, D.M. Kass, C. Newman, S.D. Guzewich, Pressure Deficit in Gale Crater and a Larger Northern Polar Cap after the Mars Year 34 Global Dust Storm. In *AGU Fall Meeting Abstracts*, **2019**, P51C-02 (2019).
49. P. Kuchynka, W.M. Folkner, A.S. Konopliv, R.S. Park, S. Le Maistre, V. Dehant, New constraints on Mars rotation determined from radiometric tracking of the opportunity Mars exploration rover. *Icarus* **229**, 340–347 (2014).
50. M. P. Panning, P. Lognonné, W. Bruce Banerdt, R. Garcia, M. Golombek, S. Kedar, B. Knapmeyer-Endrun, A. Mocquet, N. A. Teanby, J. Tromp, R. Weber, E. Beucler, J.-F. Blanchette-Guertin, E. Bozdağ, M. Drilleau, T. Gudkova, S. Hempel, A. Khan, V. Lekić, N. Murdoch, A.-C. Plesa, A. Rivoldini, N. Schmerr, Y. Ruan, O. Verhoeven, C. Gao, U. Christensen, J. Clinton, V. Dehant, D. Giardini, D. Mimoun, W. Thomas Pike, S. Smrekar, M. Wicczorek, M. Knapmeyer, J. Wookey, Planned products of the Mars structure service for the InSight mission to Mars. *Space Sci. Rev.* **211**, 611–650 (2016).
51. J. A. D.Connolly, Computation of phase equilibria by linear programming: a tool for geodynamic modeling and its application to subduction zone decarbonation. *Earth Planet. Sci. Lett.* **236**, 524–541 (2005).
52. L. Stixrude, C. Lithgow-Bertelloni, Thermodynamics of mantle minerals. Part 1: Physical properties. *Geophys. J. Int.* **162**, 610–632 (2005).
53. S. Greenwood, C.J. Davies, A. Pommier, Influence of Thermal Stratification on the Structure and Evolution of the Martian Core. *Geophysical Research Letters*, **48**(22), e2021GL095198 (2021).

54. H. Terasaki, A. Rivoldini, Y. Shimoyama, K. Nishida, S. Urakawa, M. Maki, F. Kurokawa, Y. Takubo, Y. Shibazaki, T. Sakamaki, A. Machida, Y. Higo, K. Uesugi, A. Takeuchi, T. Watanuki, T. Kondo, Pressure and Composition Effects on Sound Velocity and Density of Core-Forming Liquids: Implication to Core Compositions of Terrestrial Planets. *J. Geophys. Res. Planets* **124**, 2272–2293 (2019).
55. K. Tsuno, D. S. Grewal, R. Dasgupta, Core-mantle fractionation of carbon in Earth and Mars: The effects of sulfur. *Geochim. Cosmochim. Acta* **238**, 477–495 (2018).
56. T. Okuchi, Hydrogen partitioning into molten iron at high pressure: implications for Earth's core. *Science* **278**, 1781–1784 (1997).
57. V. Clesi, M. A. Bouhifd, N. Bolfan-Casanova, G. Manthilake, F. Schiavi, C. Raepsaet, H. Bureau, H. Khodja, D. Andrault, Low hydrogen contents in the cores of terrestrial planets. *Sci. Adv.* **4**, e1701876 (2018).
58. V. Malavergne, H. Bureau, C. Raepsaet, F. Gaillard, M. Poncet, S. Surblé, D. Sifré, S. Shcheka, C. Fourdrin, D. Deldicque, H. Khodja, Experimental constraints on the fate of H and C during planetary core-mantle differentiation. Implications for the Earth. *Icarus* **321**, 473–485 (2019).
59. L. Yuan, G. Steinle-Neumann, Strong sequestration of hydrogen into the Earth's core during planetary differentiation. *Geophys. Res. Lett.* **47**, e2020GL088303 (2020).
60. D.L. Anderson, J.B. Minster, The frequency dependence of Q in the Earth and implications for mantle rheology and Chandler wobble. *Geophys. J. R. Astron. Soc.* **58**, 431–440 (1979).
61. M. Yseboodt, R.M. Baland, S. Le Maistre, Transformation between the Martian Rotation and Orientation Angles, *Celest Mech Dyn Astr. in preparation* (2022).
62. A. S. Konopliv, R. S. Park, W. M. Folkner. An improved JPL Mars gravity field and orientation from Mars orbiter and lander tracking data. *Icarus* **274**, 253–260 (2016).
63. M. Wieczorek, Create crustal thickness maps of planets from gravity and topography (ctplanet). doi:10.5281/zenodo.4439426 (2021).
64. B. Knapmeyer-Endrun, M. P. Panning, F. Bissig, R. Joshi, A. Khan, D. Kim, V. Lekić, B. Tauzin, S. Tharimena, M. Plasman, N. Compaire, R. F. Garcia, L. Margerin, M. Schimmel, E. Stutzmann, N. Schmerr, E. Bozdağ, A.-C. Plesa, M. A. Wieczorek, A. Broquet, D. Antonangeli, S. M. McLennan, H. Samuel, C. Michaut, L. Pan, S. E. Smrekar, C. L. Johnson, N. Brinkman, A. Mittelholz, A. Rivoldini, P. M. Davis, P. Lognonné, B. Pinot, J. Scholz, S. Stähler, M. Knapmeyer, M. van Driel, D. Giardini, W. B. Banerdt, Thickness and structure of the martian crust from InSight seismic data. *Science* **373**, 438–443 (2021).
65. E. C. Thompson, A. H. Davis, W. Bi, J. Zhao, E. E. Alp, D. Zhang, E. Greenberg, V. B. Prakapenka, A. J. Campbell, High-Pressure Geophysical Properties of fcc Phase FeH_x. *Geochem. Geophys. Geosys.* **19**, 305–314 (2018).
66. P.I. Dorogokupets, A.M. Dymshits, K.D. Litasov, T.S. Sokolova, Thermodynamics and Equations of State of Iron to 350 GPa and 6000 K. *Sci. Rep.* **7**, 41863 (2017).
67. T. Komabayashi, Thermodynamics of melting relations in the system Fe-FeO at high pressure: Implications for oxygen in the Earth's core. *J. Geophys. Res.* **119**, 4164–4177 (2014).
68. F. Xu, G. Morard, N. Guignot, A. Rivoldini, G. Manthilake, J. Chantel, L. Xie, A. Yoneda, A. King, E. Boulard, S. Pandolfi, F.J. Ryerson, D. Antonangeli, Thermal expansion of liquid Fe-S alloy at high pressure. *Earth and Planetary Science Letters* **563** (2021).
69. G. Morard, J. Siebert, D. Andrault, N. Guignot, G. Garbarino, F. Guyot, The Earth's core composition from high pressure density measurements of liquid iron alloys. *Earth Planet. Sci. Lett.* **373**, 169–178 (2013).
70. S. Kawaguchi, Y. Nakajima, K. Hirose, T. Komabayashi, H. Ozawa, S. Tateno, Y. Kuwagama, S. Tsutsui, A.Q.R. Baron, Sound velocity of liquid Fe–Ni–S at high pressure. *J. Geophys. Res. Solid Earth* **122**, 3624–3634 (2017).
71. K. Nishida, Y. Shibazaki, H. Terasaki, Y. Higo, A. Suzuki, F. Nobumasa, K. Hirose, Effect of sulfur on sound velocity of liquid iron under Martian core conditions. *Nat Commun* **11**, 1954 (2020).

72. G.H., Kaiura, J.M., Toguri, Densities of the molten FeS, FeS–Cu₂S and Fe–S–O systems—utilizing a bottom-balance Archimedean technique. *Can. Metall. Quart.* **18**(2), 155-64 (1979).
73. M.W. Chase, NIST-JANAF Thermochemical Tables Fourth, J. Phys. Chem. Ref. Data Monograph **9** (1998).
74. Y. Shimoyama, H. Terasaki, S. Urakawa, Y. Takubo, S. Kuwabara, S. Kishimoto, T. Watanuki, A. Machida, Y. Katayama, T. Kondo, Thermoelastic properties of liquid Fe–C revealed by sound velocity and density measurements at high pressure. *J. Geophys. Res., Solid Earth* **121**(11), 7984–7995 (2016).
75. H. Terasaki, K. Nishida, Y. Shibazaki, T. Sakamaki, A. Suzuki, E. Ohtani, T. Kikegawa, Density measurement of Fe₃C liquid using X-ray absorption image up to 10 GPa and effect of light elements on compressibility of liquid iron. *J. Geophys. Res.: Solid Earth* **115**, B06207 (2010).
76. G. Morard, Y. Nakajima, D. Andrault, D. Antonangeli, A. L. Auzende, E. Boulard, S. Cervera, A. N. Clark, O. T. Lord, J. Siebert, V. Svitlyk, G. Garbarino, M. Mezouar, Structure and Density of Fe-C Liquid Alloys Under High Pressure. *J. Geophys. Res. Solid Earth* **122**, 7813–7823 (2017).
77. A.-C. Plesa, S. Padovan, N. Tosi, D. Breuer, M. Grott, M. A. Wieczorek, T. Spohn, S. E. Smrekar, and W. B. Banerdt, The thermal state and interior structure of Mars, *Geophys. Res. Lett.* **45**, 12198-12209 (2018).
78. A. Khan, S. Ceylan, M. van Driel, D. Giardini, P. Lognonné, H. Samuel, Ni. C. Schmerr, S. C. Stähler, A. C. Duran, Q. Huang, D. Kim, A. Broquet, C. Charalambous, J. F. Clinton, P. M. Davis, M. Drilleau, F. Karakostas, V. Lekic, S. M. McLennan, R. R. Maguire, C. Michaut, M. P. Panning, W. T. Pike, B. Pinot, M. Plasman, J.-R. Scholz, R. Widmer-Schnidrig, T. Spohn, S. E. Smrekar, W. B. Banerdt, 2021, Upper mantle structure of Mars from InSight seismic data. *Science*. **373** (6553), 434-438 (2021).
79. M.A. Wieczorek, M. Meschede, SHTools: tools for working with spherical harmonics. *Geochem. Geophys. Geosyst.* **19**, 2574–2592 (2018).
80. D. Kim, V. Lekić, J. C. E. Irving, N. Schmerr, B. Knapmeyer-Endrun, R. Joshi, M. P. Panning, B. Tauzin, F. Karakostas, R. Maguire, Q. Huang, S. Ceylan, A. Khan, D. Giardini, M. A. Wieczorek, P. Lognonné, W. B. Banerdt. Improving constraints on planetary interiors with PPS receiver functions. *Journal of Geophysical Research: Planets*, **126**(11), e2021JE006983 (2021).
81. P.M. Mathews, T.A. Herring, B.A. Buffett, Modeling of nutation precession: new nutation series for non-rigid Earth, and insights into the Earth's interior. *J. Geophys. Res.* **107**, 2068 (2002).
82. B.A. Buffett, U.R. Christensen, Magnetic and viscous coupling at the core-mantle boundary: Inferences from observations of Earth's nutations. *Geophys. J. Int.* **171**, 143-152 (2007).
83. M Puica, V Dehant, M Folgueira, T Van Hoolst, and J Requier. Analytical computation of total topographic torque at the core-mantle boundary and its impact on tidally driven length-of-day variations. *Geophysical Journal International*, **234**,585-596, 02 (2023).
84. W. Chen, WenBin Shen, New estimates of the inertia tensor and rotation of the triaxial nonrigid earth. *Journal of Geophysical Research: Solid Earth*, **115**(B12), (2010).
85. V.N. Zharkov, T.V. Gudkova, S.M. Molodensky, On models of Mars interior and amplitudes of forced nutations: 1. The effects of deviation of Mars from its equilibrium state on the flattening of the core-mantle boundary. *Phys. Earth Planet. Inter.* **172**(3), 324–334 (2009).
86. H. Moritz, Ed., *The Figure of the Earth: Theoretical Geodesy and the Earth's Interior* (Wichmann, Karlsruhe, 1990).
87. M. Greff-Lefftz, H. Legros, Some remarks about the degree-one deformation of the Earth, *Geophys. J. Int.*, **131**, 699-723 (1997).
88. M. A. Richards, B. H. Hager, Geoid anomalies in a dynamic Earth, *J. Geophys. Res.* **89**, B7, 5987-6002 (1984).
89. P. Defraigne, V. Dehant, J. M. Wahr, Internal loading of an inhomogeneous compressible earth with phase boundaries, *Geophys. J. Int.* **125**, 173-192 (1996).
90. S. V. Panasyuk, B. H. Hager, A. M. Forte, Understanding the effects of mantle compressibility on geoid kernels, *Geophys. J. Int.* **124**, 121-133 (1996).

91. A. Broquet, M. A. Wicczorek, W. Fa, Flexure of the Lithosphere Beneath the North Polar Cap of Mars: Implications for Ice Composition and Heat Flow. *Geophys. Res. Lett.* **47**, e2019GL086746 (2020).
92. L.T. Elkins-Tanton, E.M. Parmentier, P.C. Hess, Magma ocean fractional crystallization and cumulate overturn in terrestrial planets: implications for Mars, Meteorit. *Planet. Sci.*, **38**, 1753-1771 (2003).
93. M.D. Ballmer, D.L. Lourenago, K. Hirose, R. Caracas, R. Nomura, Reconciling magma-ocean crystallization models with the present-day structure of the Earth's mantle. *Geochem Geophys Geosyst* **18**, 2785–2806 (2017).
94. C.-E. Boukaré, E.M. Parmentier, S.W. Parman, Timing of mantle overturn during magma ocean solidification, *Earth Planet. Sci. Lett.* **491**, 216-22 (2018).
95. M. Maurice, N. Tosi, H. Samuel, A.-C. Plesa, C. Hüttig, D. Breuer, Onset of solid-state mantle convection and mixing during magma ocean solidification. *J. Geophys. Res. Planets* **122**, 577–598 (2017).
96. H. Samuel, P. Lognonné, M. Panning, V. Lainey, The rheology and thermal history of Mars revealed by the orbital evolution of Phobos. *Nature* **569**, 523–527 (2019).
97. W.K. Hartmann, M. Malin, A. McEwen, M. Carr, L. Soderblom, P. Thomas, E. Danielson, P. James, J. Veverka, Evidence for recent volcanism on Mars from crater counts, *Nature* **397**, 586-590 (1999).
98. G. Neukum, R. Jaumann, H. Hoffmann, E. Hauber, J.W. Head, A.T. Basilevsky, T. McCord, Recent and episodic volcanic and glacial activity on Mars revealed by the High Resolution Stereo Camera. *Nature*, **432**(7020), 971-979 (2004).
99. J. A. D. Connolly, The geodynamic equation of state: What and how. *Geochem. Geophys. Geosyst.* **10**, 10 (2009).
100. F. Nimmo, U.H. Faul, Dissipation at tidal and seismic frequencies in a melt-free, anhydrous Mars. *J. Geophys. Res.* **118**(12), 2558–2569 (2013).
101. A.M. Lejeune, P. Richet, Rheology of crystal-bearing silicate melts: an experimental study at high viscosities, *J. Geophys. Res.* **100**, 4215-4229 (1995).
102. D. Yamazaki, S. Karato, Some mineral physics constraints on the rheology and geothermal structure of earth's lower mantle, *Am. Mineralog.* **86**(4), 385-391 (2001).
103. M. Drilleau, H. Samuel, A. Rivoldini, M. Panning, P. Lognonné, Bayesian inversion of the Martian structure using geodynamic constraints. *Geophys. J. Int.* **226**, 1615–1644 (2021).
104. K. Lodders, B. Fegley, Jr An oxygen isotope model for the composition of Mars. *Icarus* **126**, 373–394 (1997).
105. G.J. Taylor, The bulk composition of Mars. *Chem. Erde* **73**(4), 401–420 (2013).
106. Y. Li, R. Dasgupta, K. Tsuno, B. Monteleone, N. Shimizu, Carbon and sulfur budget of the silicate Earth explained by accretion of differentiated planetary embryos. *Nat. Geosci.* **9**, 781–785 (2016).
107. G. Morard, S. Boccato, A.D. Rosa, S. Anzellini, F. Miozzi, L. Henry, G. Garbarino, M. Mezouar, M. Harmand, F. Guyot, E. Boulard, I. Kantor, T. Irifune, R. Torchio, Solving controversies on the iron phase diagram under high pressure. *Geophys. Res. Lett.* **45**, 11074-11082 (2018).
108. Y. Mori, H. Ozawa, K. Hirose, R. Sinmyo, S. Tateno, G. Morard, Y. Ohishi, Melting experiments on Fe-Fe₃S system to 254 GPa. *Earth Planet. Sc. Lett.* **464**, 135-141 (2017).
109. Y. Fei, E. Brosh, Experimental study and thermodynamic calculations of phase relations in the Fe–C system at high pressure. *Earth Planet. Science Lett.* **408**, 155–162 (2014).
110. Y. Shibazaki, H. Terasaki, E. Ohtani, R. Tateyama, K. Nishida, K. Funakoshi, Y. Higo, High-pressure and high-temperature phase diagram for Fe_{0.9}Ni_{0.1}–H alloy. *Phys. Earth Planet. Inter.* **228** (2014), 192-201 (2014).